Project No. 10-857

Carbide Coatings for Nickel Alloys, Graphite and Carbon/Carbon Composites to be used in Fluoride Salt Valves

Reactor Concepts

Denis Nagle
Johns Hopkins University

In collaboration with:
None

Brian Robinson, Federal POC
Tim Burchell, Technical POC

NEUP Nuclear Energy University Programs
U.S. Department of Energy

The Johns Hopkins University

Carbide Coatings for Nickel Alloys, Graphite and Carbon/Carbon Composites to Be Used in Fluoride Salt Valves

Final Report

October 22, 2015

Prepared for:

DOE NEUP

Prepared by:

Principle Investigators:

Dr. Dennis Nagle

Dr. Dajie Zhang

Table of Contents

List of Tables:

List of Figures:

21. Tube Furnace CVD Apparatus
22. Sample Surface Temperature Measurement
23. XRD results for chromium films subjected to CVD process in the temperature range of 900°C-1000°C
24. Inconel Retort CVD Apparatus
25. XRD results for chromium films subjected to the CVD process outlined above at 1000°C and 1050°C
26. XRD patterns of the Cr_2O_3 feedstock powder used in this work (top scan) and the resulting plasma-sprayed coating (bottom scan), indicating no appreciable compositional changes as a result of the deposition process.
27. Cross-sectional SEM micrograph of plasma-sprayed Cr_2O_3 (top coat), showing a complex pore structure containing globular voids, interlamellar porosity and intralamellar microcracks.
28. XRD patterns of plasma-sprayed Cr_2O_3 after various reduction times (0.1-0.3 h) at 1000ºC, showing coating phase evolution from Cr_2O_3 to binder-free Cr_3C_2.
29. Cross-sectional SEM micrographs of plasma-sprayed Cr_2O_3 after various reduction times at 1000 ºC, illustrating characteristics of the mechanism of reduction to binder-free Cr_3C_2: (a) 0.1 h, (b) 0.2 h, (c) 0.3 h.
30. Void formation in the Cr_3C_2 phase formed from the reduction of plasma-sprayed Cr_2O_3. Label "A" corresponds to unconverted Cr_2O_3 and label "B" corresponds to newly-formed microporous Cr_3C_2.
31. XRD coating phase evolution of an electrodeposited Cr coating after 6 and 12 h of post-treatment with methane-containing gas at 1000 °C.
32. SEM micrograph of coating porosity in an (a) electrodeposited Cr coating, (b) electrodeposited Cr coating after 6 h of post-treatment with methane-containing gas at 1000 °C and (c) electrodeposited Cr coating after 12 h of post-treatment with methane-containing gas at 1000°C.
33. XRD coating phase evolution of a plasma-sprayed Cr coating after 6 and 12 h of post-treatment with methane-containing gas at 1000 °C.
34. SEM micrograph of coating porosity in a (a) plasma-sprayed Cr coating, (b) plasma-sprayed Cr coating after 6 h of post-treatment with methane-containing gas at 1000 °C and (c) plasma-sprayed Cr coating after 12 h of post-treatment with methane-containing gas at 1000 °C.
35. XRD coating phase evolution of a cold-sprayed Cr coating after 6 and 12 h of post-treatment with methane-containing gas at 1000 °C.
36. SEM micrograph of coating porosity in a (a) cold-sprayed Cr coating, (b) cold-sprayed Cr coating after 6 h of post-treatment with methane-containing gas at 1000°C and (c) cold-sprayed Cr coating after 12 h of post-treatment with methane-containing gas at 1000°C.

1.0 Executive Summary

The focus of this research was concerned with developing materials technology that supports the evolution of Generation IV Advanced High Temperature Reactor (AHTR) concepts. Specifically, we investigate refractory carbide coatings for 1) nickel alloys, and 2) commercial carbon-carbon composites (CCCs). Numerous compelling reasons have driven us to focus on carbon and carbide materials. First, unlike metals, the strength and modulus of CCCs increase with rising temperature. Secondly, graphite and carbon composites have been proven effective for resisting highly corrosive fluoride melts such as molten cryolite [Na_3AlF_6] at ~1000^{o}C in aluminum reduction cells. Thirdly, graphite and carbide materials exhibit extraordinary radiation damage tolerance and stability up to 2000°C. Finally, carbides are thermodynamically more stable in liquid fluoride salt than the corresponding metals (i.e. Cr and Zr) found in nickel based alloys.

Early in our research, we focused on four coating processes: [1] liquid metal infiltration of porous graphite and other carbon materials, [2] molten salt deposition of carbides on graphite and carbon/carbon composites, [3] Vapor phase carbide formation using metal carbonyl precursors, and [4] Refractory carbide coating of nickel alloys with a modified vapor phase carburization process. The first three coating processes were judged not to be of a quality that could survive the corrosion environment expected for molten salt baths. This allowed us to focus on the fourth process of formation of pure chromium carbide coatings on nickel alloys. Initially, we developed processes for deposition of chromium metal by (1) electrochemical plating (2) plasma spray and (3) cold spray techniques on the nickel alloys and subsequently converted these metal coatings to chromium carbide by a CVD method using methane gas mixtures. Complete conversion to chromium carbide (Cr_3C_2) at 1000°C was achieved after 6 to 12 hours of exposure

In the course of these carbide conversion experiments, it was discovered that the conversion process was highly sensitive to the presence of oxygen. Without oxygen, the conversion process is essentially stopped. Based on these observations, we initiated CVD experiments to convert plasma sprayed chromium oxide to chromium carbide. These experiments demonstrated that chromium oxide coatings on nickel can be completely converted to chroiume carbide in less than 18 minutes at 1000°C. These observations are the basis of several patent disclosures being filed (See patent disclosures in Appendix).

In our corrosion study, chromium carbide coatings produced by conversion of plasma sprayed chromium oxide and cold sprayed chromium metal were exposed to molten fluoride salts for approximately 250 hours. These coatings de-bonded in several areas. It is believed that the molten salt was able to penetrate the porous carbide in these areas corroding the base metal resulting in the observed de-bonding. This failure mode is often seen in ceramic thermal barrier coatings when a corrosion resistant bond layer is not used. Future research should focus reducing the porosity of the chromium carbide and on developing a corrosion resistant bond layer.

2.0 Introduction

Several next-generation AHTR designs incorporate molten fluoride salts as the heat exchanger cooling fluid. Considerable research has been conducted on nickel based alloys for salt containment to assess and mitigate the severe corrosion challenges of these working fluids on valve, piping, and vessel materials. While there certainly is justification for pursuing molten salt compatible superalloy systems, advanced carbon based materials available today present an alternate path for mitigating the fundamental limitations of these superalloys. We have investigated a number of carbon and carbide-based systems for molten salt containment. Specifically, we are investigating refractory carbide coatings for 1) nickel alloys and 2) commercial carbon-carbon composites (CCCs). Numerous compelling reasons have driven us to focus on carbon and carbide materials. First, unlike metals, the strength and modulus of CCCs increase with rising temperature. Secondly, graphite has been proven effective for resisting highly corrosive fluoride melts such as molten cryolite [Na_3AlF_6] at ~1000^{o}C in aluminum reduction cells. These reduction cells contain graphite cathodes that operate continuously for 7-10 years before being replaced. The nature of their eventual failure has been studied and attributed to further graphitization of the cathode catalyzed by the sodium ions and swelling caused by sodium intercalation of the graphite. Molten aluminum and cryolite also slowly erode the uncoated graphite. Thirdly, graphite and carbide materials exhibit extraordinary radiation damage tolerance and stability up to 2000°C, which is paramount for high temperature radioactive environments. Finally, carbides are thermodynamically more stable in liquid fluoride salt than the corresponding metals (i.e. Cr, Mo, Zr) found in nickel based alloys.

Our research was aimed at [1] better understanding the corrosion mechanisms of graphite, CCCs and carbide-coated super alloys in the presence of molten fluoride salt bath compositions at expected heat exchanger temperatures, [2] developing carbide coating techniques, [3] demonstrating and quantifying erosion protection with carbide coatings. We will demonstrate that these refractory coatings can be formed by several techniques including: [1] liquid metal infiltration of porous graphite and other carbon materials, [2] molten salt deposition of carbides on graphite, carbon/carbon composites or alloys, [3] vapor phase formation using metal carbonyl precursors, and [4] refractory carbide coating of nickel alloys with a modified vapor phase carburization process.

2.1 Path for Achieving Goals and Task Description

The degradation of graphite, CCCs and nickel alloys due to molten fluoride exposure can be examined for extended time periods at realistic temperatures to determine [1] the mechanisms by which they are attacked by the salts, and [2] the rate at which it occurs. For our studies we propose to use the LiF-NaF-KF molten salt used in prior superalloy corrosion studies. Materials for molten salt corrosion studies will be coated with chromium carbide. In the case of the CCCs, we will also make similar composites where the glassy carbon matrix phase formed from phenolic resin binders will be modified using microcrystalline cellulose additions. This will alter the porosity of the glassy carbon phase formed during carbonization to create an engineered pore topology optimized for creating fully dense, well-bonded carbide coatings. Carbide coatings will be characterized by optical and SEM methods to determine their overall quality based on uniformity and porosity. After molten salt exposure testing each sample will be characterized again for depth of corrosion and salt penetration using SEM/EDX and optical microscopy. In addition, chemical analysis of the salt bath will be conducted to determine the concentrations of leached metal ions in the salt bath. Based on our research findings we will identify the critical issues associated with degradation of carbide-coated graphite and metal alloys, contrasted with the baseline materials. The materials developed will be examined for their potential for creating high performance structures suitable for nuclear heat exchanger applications such as valves.

3.0 Coating Processes

The coating processes we have investigated included: [1] liquid metal infiltration of porous graphite and other carbon materials, [2] molten salt deposition of carbides on graphite, carbon/carbon composites or alloys, [3] Chemical vapor phase formation using metal carbonyl precursors, and [4] Refractory carbide coating of nickel alloys with a modified vapor phase carburization process.

3.1 Liquid Metal Infiltration and Plasma Spray coatings

The use of liquid metal infiltration of porous carbons has been very effective in conversion of carbon surfaces to metal carbides. We have had extensive experience using silicon metal to form a protective coating on carbon as well as converting the entire carbon structure to

silicon carbide at temperatures below 1600°C. We have also had some success with conversion of the surface of carbon to zirconium carbide at temperatures above the melting point of zirconium [1855°C]. However, the high vapor pressure of carbon becomes an issue. The carbon diffuses to the refractory metal to form a carbide before the metal melts resulting in little and in some cases no liquid phase since the carbides have much high melting points than the refractory metal.

To alleviate this problem, we started our experiment by coating carbon-carbon composite coupons with a thin layer (3-5 mil) of metal (Ti, Nb, Ta, W) by the means of thermal plasma spray, followed by thermal treatment at 1400°C inside a vacuum furnace for 6-12 hours. This allows the inter diffusion between the carbon and refractory metal to form the carbide. Figures 1 -3 present examples of X-ray power diffraction (XRD) patterns of Nb, Ti, and a mixture of 80%W + 20%Ta plasma sprayed coatings after heat treatment. These figures show that except for W, all the other metals react with carbon to form carbides under such conditions.

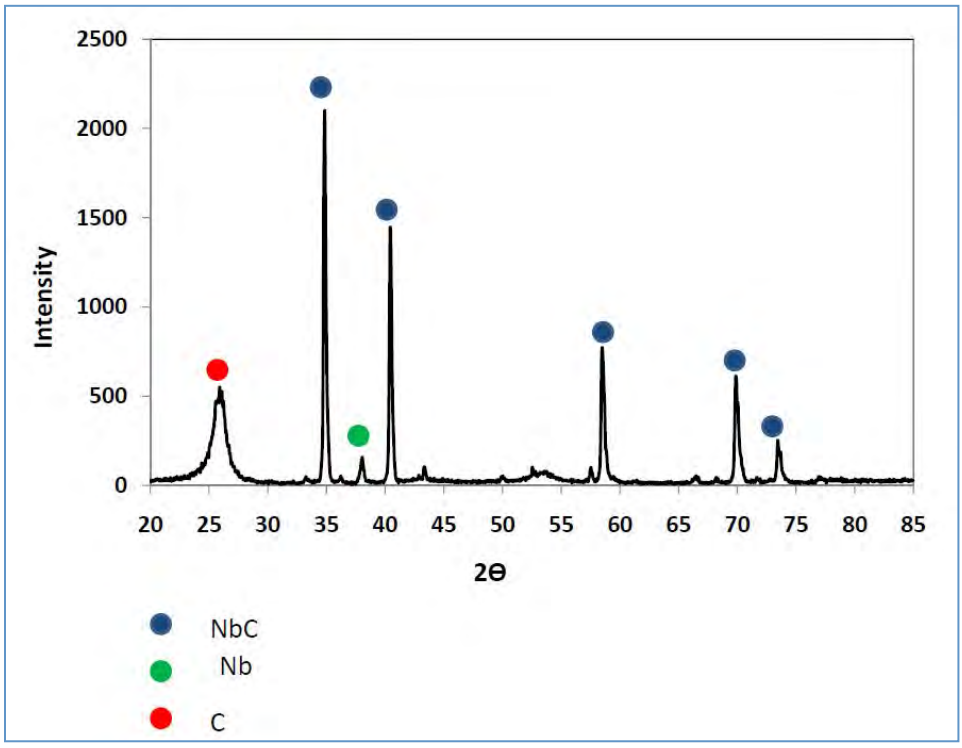

Figure 1. XRD pattern of plasma-sprayed Nb coating on C-C composite heat-treated at 1400°C in vacuum.

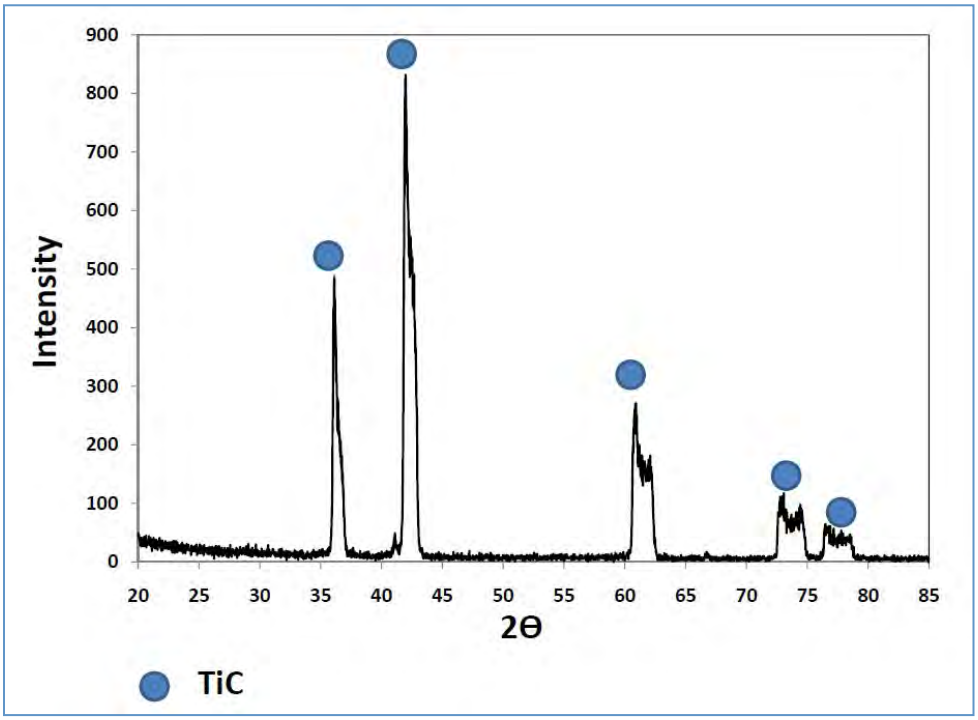

Figure 2. XRD pattern of plasma-sprayed Ti coating on C-C composite heat-treated at 1400°C in vacuum.

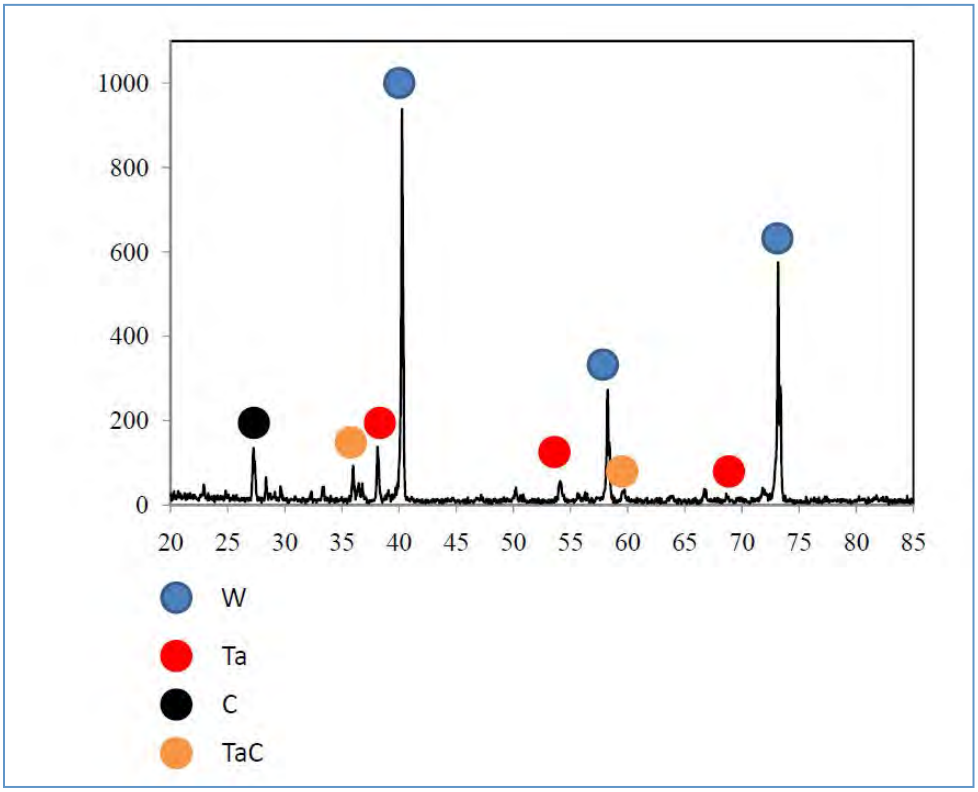

Figure 3. XRD pattern of plasma-sprayed 80%W + 20%Ta coating on C-C composite heat-treated at 1400°C in vacuum.

3.2 Molten Salt Deposition of Carbides

Due to the technical importance, the studies on the formation of refractory carbide coatings and nano-powders have been an active field for several decades. Various techniques have been investigated for carbide coating formation, which include molten salt bath deposition, sol-gel reactive coating, chemical vapor deposition and laser assisted deposition. Molten salt bath deposition method is the mostly studied method due to its simplicity and ease of scale-up. Although molten salt bath deposition can be either an electro-deposition or an electro-less deposition process, most of the studies on molten salt bath carbide deposition were carried out using electro-deposition techniques. Salt bath electro-deposition has been successfully employed in industrial applications in refining metallic elements including active metals such as sodium, calcium, lithium, aluminum, titanium and magnesium [1]. In theory, this method can also be an effective approach in depositing coatings of refractory metals such as hafnium, niobium, tantalum and vanadium and their carbides on certain types of substrate materials. These substrates can either be inert or reactive towards the metal coatings formed by the electrolysis. When an inert substrate is used, a metal coating is formed. If a reactive substrate is used, then a carbide coating is obtained through the reaction of the substrate and the electro-deposited metal.

Electro-deposition of refractory metals and their carbides from molten salts has been studied by many teams and the molten salt systems are mainly alkaline halide eutectic mixtures [3-6]. Fluoride systems were mostly favored because of the low vapor pressures of the salts and the reactive metal fluorides. The most studied fluoride molten salt melt is the ternary eutectic LiF-NaF-KF (FLINAK) due to its low melting point of 453 °C, but refractory metals cannot be successfully deposited from FLINAK below 700 °C and reaction temperatures above 700 °C are needed [7]. K.H. Stern has successfully deposited Mo_2C, Ta_2C and W_2C from FLINAK with carbonate as the carbon source [7]. The deposition of Ti, Zr, V, Nb, and Cr carbides was also attempted but all not successful. Stern attributed the failures mainly due to the formation of insoluble metal oxide species formed during the reaction and possible low reaction temperatures (750 °C). More recent research efforts have been strongly directed to employing chloride molten salt melt mainly due to the fact that fluoride molten salts are very corrosive towards many reactor vessel materials, especially at high temperatures. However, as mentioned earlier, many of the precursor materials have high vapor pressures in chloride melts; and for some of the most

important refractory metals such as hafnium, zirconium, niobium and tantalum, the boiling (sublimation) points of their chlorides are well below 320 °C, which make it hard to deposit these metals and their carbides from chloride molten salt bath due to the sublimation (vaporization) of the precursors.

Although electro-less molten salt bath deposition process has not been widely studied for its application for refractory carbide deposition, it has been commercially applied to form carbide coatings on metals and alloys. In high temperature molten salt bath, the presence of metal ions presences a mobile and reactive medium enabling both thermo-chemical reactions and electro-chemical deposition. While electro-deposition is driven by electrical energy, electro-less thermo-chemical reaction in molten salt bath is a type of self-propagating process that is driven by the chemical reactivity of supersaturated ionic species and/or the substrate materials. Electro-less molten salt bath thermo-chemical reaction improves on the traditional solid-phase Self-Propagating Synthesis (SHS) technique by using solvated metal ion in a thermally moderating solvent to synthesize metal and inter-metallic matrix composites through reactions. Such controlled deposition process was first developed by Toyota to form a wear-resistant layer of carbides, nitrides, or carbonitrides and was initially called Toyota Diffusion (TD) coating process and later named the Thermo-reactive Deposition / Deposition Process (TRD) [8]. In the TRD process, the carbon and nitrogen in steel substrate diffuse onto the surface and react with a carbide forming or nitride forming element such as vanadium, niobium, tantalum, chromium, molybdenum, or tungsten, to form a dense and atomically bonded carbide or nitride coating at the substrate surface. Sodium tetra-borate or boric acid is often the main solvent for this process, and either elemental metals or metal salts can be added to the melt. When metal salts are used, a reducing agent is also added to provide electrons for the reaction. For example, in the formation of vanadium carbide coatings on high carbon steel from a boric acid molten salt bath, vanadium oxide is dissolved along with an iron silicon alloy, and the iron silicon alloy reacts with vanadium oxide to form elemental vanadium and iron silicates. The elemental vanadium produced is soluble in the molten boric oxide and it reacts with carbon in steel to form the carbide coatings at 1000 °C according to the reaction [9]:

$$\text{FeSi alloy} + V_2O_5 + C \rightarrow Fe_2O_3 + SiO_2 + 2VC$$

Vanadium carbide up to 1 mil (25 μm) in thickness can be formed by such process.

We have explored the used of both fluoride and chloride molten salt baths for electro-deposition and electro-less depositions of refractory metals and their carbides on graphite and carbon fiber surfaces.

3.2.1 Fluoride and chloride molten salt bath systems in open reactors

When working with fluoride molten salt bath systems (NaF + KF), we have encountered delaminating of C-C composite. In the chloride approach, by using a 1:1 molar ratio NaCl and KCl molten salt eutectic melt with hafnium metal as the anode, we have successfully deposit hafnium carbide on C-C composite at 900°C in an alumina reactor (Figure 4). However, during the reaction we observed the loss of hafnium due to the sublimation of hafnium as hafnium chloride. Electro-less deposition of hafnium carbide on C-C composite was also successful with NaCl melt dissolved $HfCl_4$ and Hf metal. Hf loss was also observed and only a thin layer of HfC coating was formed before the reaction was terminated by the total loss of $HfCl_4$ from the melt.

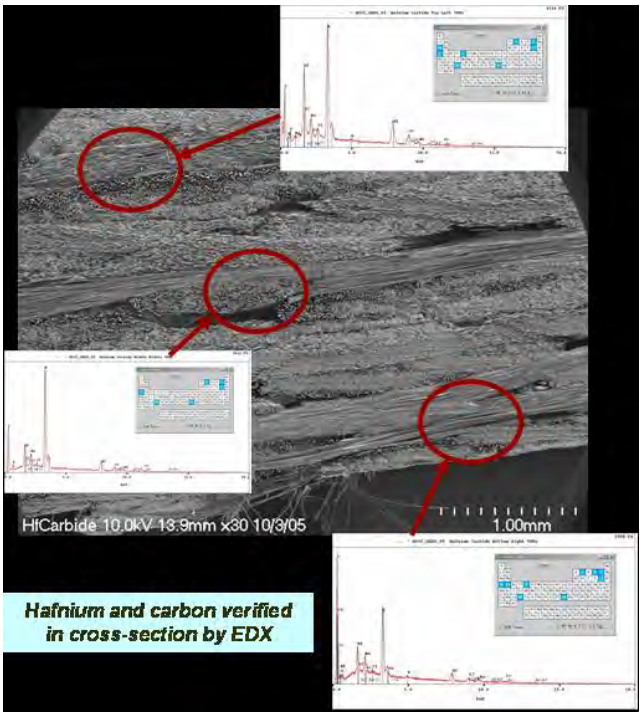

Figure 4. Elemental analysis (EDX) shows the formation of HfC on C-C composite.

3.2.2 Chloride molten salt bath systems in sealed reactors

In order to prevent the sublimation of metal chlorides, we used sealed metal reactors. This high temperature electrochemical reactor was designed to electrochemically deposit carbide coatings onto carbon and nickel substrates. To form a carbide coating on the nickel alloys, the nickel must first be carburized at high temperatures. The electrochemical process will then deposit the refractory metal dissolved in the molten to the nickel alloy surface to from the carbide coating.

All electrodeposited coatings were developed in a molten salt electrochemical reactor that was designed and fabricated on-site. The reactor consists of a Stainless Steel (316) containment tube, measuring 4.25" in diameter and 48" tall, positioned vertically in an electrical resistance tube furnace. The reactor is sealed by means of a welded-on Stainless Steel (316) flange and a bolted on Stainless Steel (316) lid. A compressible Silicone gasket between the flange and lid ensures that the reactor is air-tight. Machined ports on the lid provide access to the inside of the reactor for argon inlet/outlets, an Inconel sheathed K-type thermocouple, and three PTFE flanged linear sleeve bearings. Figure 5 shows the fabricated reactor positioned within the vertical tube furnace.

Figure 5: Electrodeposition reactor.

A pair of Inconel rods of 1/8” diameter and an alumina tube of matching diameter are inserted into the reactor by means of the PTFE flanged sleeve bearings. The Inconel rods function as leads for the cathode/anode and the alumina tube ensures electrical isolation of a reference electrode to be used in future voltammetric studies. Inconel lead holders are welded onto the end of each Inconel rod and function as electrical conductors to which the cathode/anode can be mechanically connected. This method of connection provides the ability to vary both substrate and sacrificial materials, which greatly increases the functionality of the reactor. It also provides a junction at which spacers may be added between the lead holders and cathode/anode, providing precise control of the cathode/anode distance if adjustment is deemed necessary. Figure 6 contains a solid model of the reactor inside which illustrates these features.

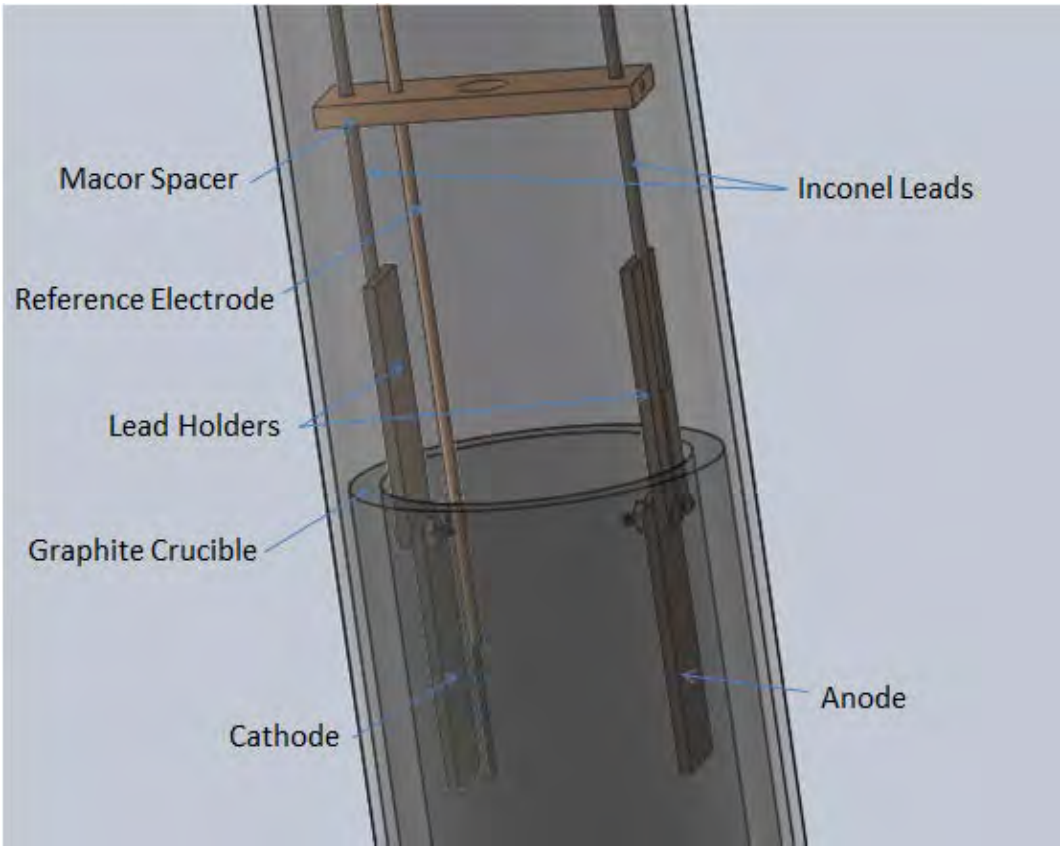

Figure 6: Solid model of the positioning of cathode/anode inside the electrodeposition reactor.

The cathode/anode distance is held constant over the depth of the reactor by means of two electrically insulating spacers, one inside of the reactor as well as one on the outside. The spacer on the outside of the reactor is made of Nylon 6/6, and the spacer on in the inside of the reactor which will be subjected to temperatures up to 1100°C is made of Macor. By using Stainless Steel set screw shaft collars with PTFE insulating cores along with the nylon spacer the depth of the cathode/anode into the reactor can be adjusted and fixed. This provides precise control of the cathode/anode area immersed in molten salt and a means by which the samples can be removed from the salt while it is still molten. FLiNaK, the molten salt to be used as an electrolyte for all deposition experiments, is contained within a graphite crucible positioned inside the reactor. Figures 7 and 8 contain solid models which illustrate these features.

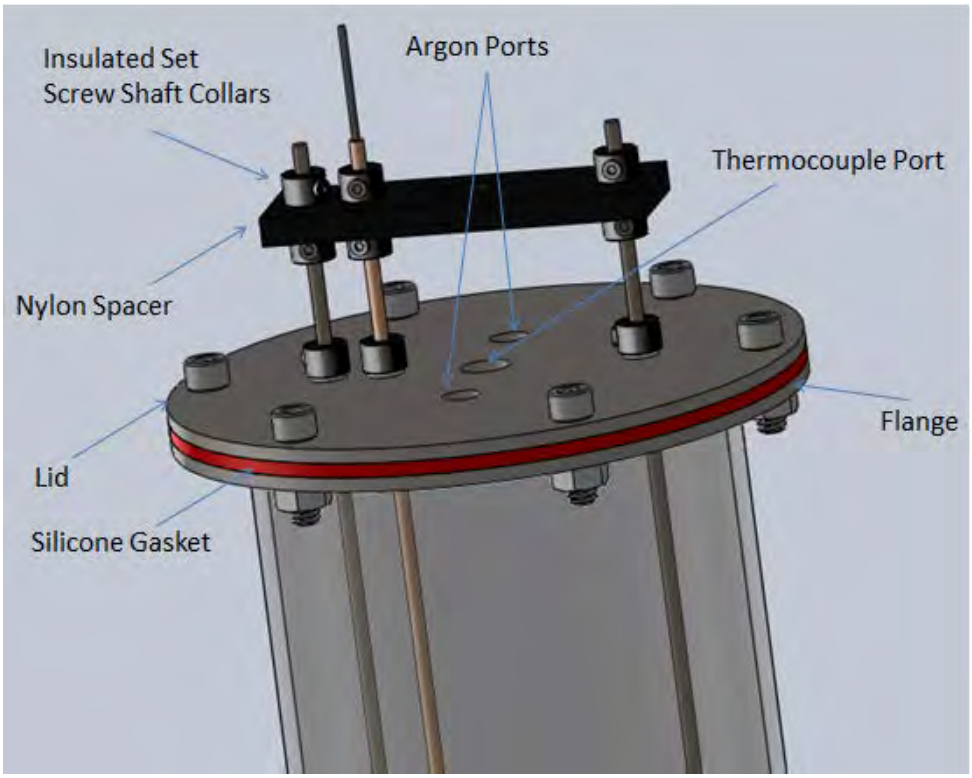

Figure 7: Solid model of the top of the electro-deposition reactor.


Figure 8: Electrodeposition reactor.

Using this sealed high temperature electro-deposition reactor, we successfully deposited ZrC on C-C composite (Figure 9) and on microcrystalline cellulose carbon (Figures10 and 7).

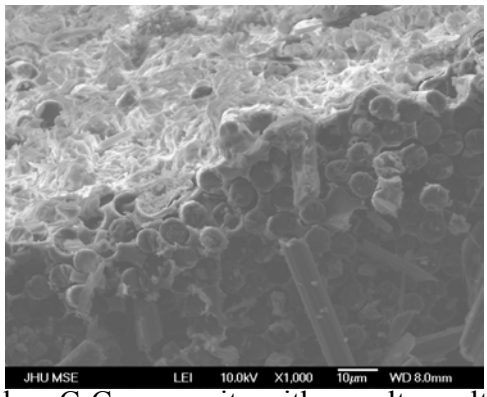

Figure 9. ZrC coating formed on C-C composite with a molten salt bath method.

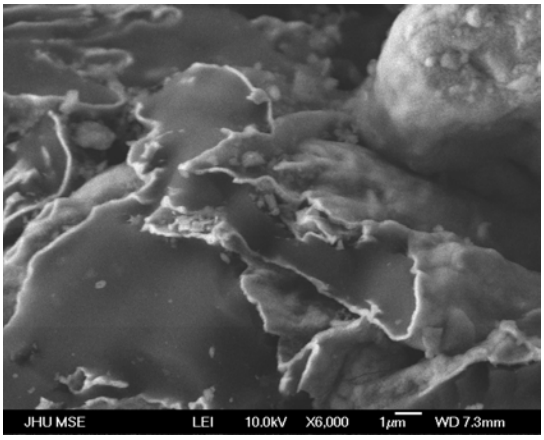

Figure 10. ZrC carbide coating formed on carbon prepared from microcrystalline cellulose.

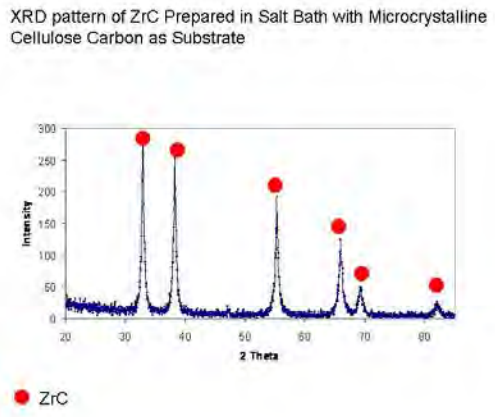

Figure 11. XRD pattern verifies the formation of ZrC on microcrystalline cellulose carbon.

3.2.2 The Development of the Chemical Vapor Transport(CVT) Process for the Formation of Carbide Coatings and Nanoparticles

By examining the results from the salt bath reactions, we concluded that the electro-less coating reactions in the chloride molten salt bath process can occur without the use of a molten salt bath due to the high vapor pressure of the reactive metal halides. In order to drive the reaction forward, metal must be present together with metal halide to first form a more reactive

and meta-stable gaseous species, and this meta-stable species disproportionate on the surface of carbon substrate to release meta atoms to react with carbon to form carbide. By using Hf system as an example, the reactions involved in the electro-less deposition process could be:

$$Hf_{(solid)} + HfCl_{4\,(gas)} \leftrightarrow 2HfCl_2^{*}{}_{(gas)}$$

$$2HfCl_2^{*}{}_{(gas)} + C_{(solid)} \rightarrow HfC_{(solid)} + HfCl_{4\,(gas)}$$

The reactions proposed above are highly simplified and other transient species such as $HfCl_3^{*}$ can also be present. Schematics of such reaction for the formation of carbide coatings and carbide nanoparticles are show in Figures 12(a) and 12(b).

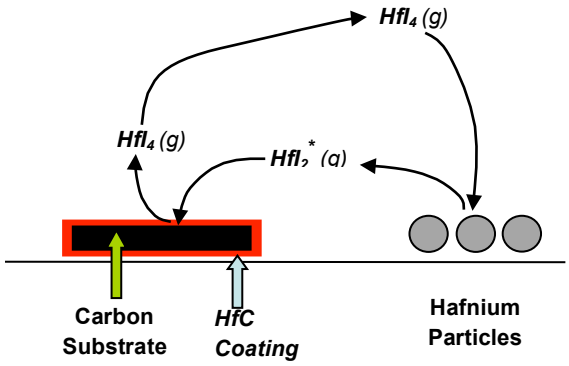

Figure 12 (a). Formation of HfC coating with the chemical vapor transport process.

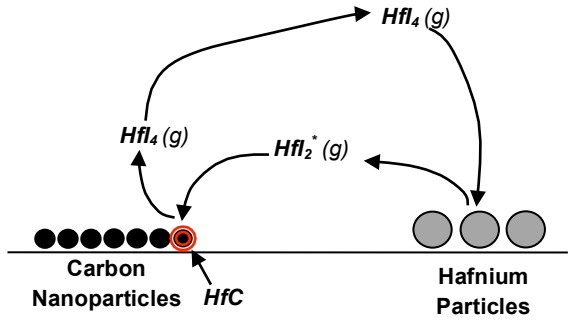

Figure 12 (b). Formation of HfC nanoparticles with the chemical vapor transport process.

We believe that such technique, named the Chemical Vapor Transport (CVT) process**,** is a major breakthrough in the formation of carbide coatings and nanocarbide materials. The starting materials and equipment are relatively inexpensive and the procedure straight forward. In this generic CVT process high surface carbon with a nano-crystalline structure is sealed in a retort with a metal forming carbide, and a small amount of a metal halide such as chloride or iodide. The retort is heat to temperatures ranging from 700°C to 1000°C for up to 24 hours. The metal halide reacts with the nano-crystalline carbon to form the desired carbide. Gaseous elemental halide is the by-product that is then available to react with the excess metal to from more metal halide allowing the reaction cycle to repeat. Excess metal over that necessary to convert all the

carbon to the carbide is necessary due to the presence of any metal oxide coating on the metal powder.

By employing the CVT process, we have produced NbC and ZrC coatings on carbon fibers and C-C composites (Figures 13, 14, 15). These reactions were all carried out at in sealed steel tubes at temperatures between 850 to 950 °C.

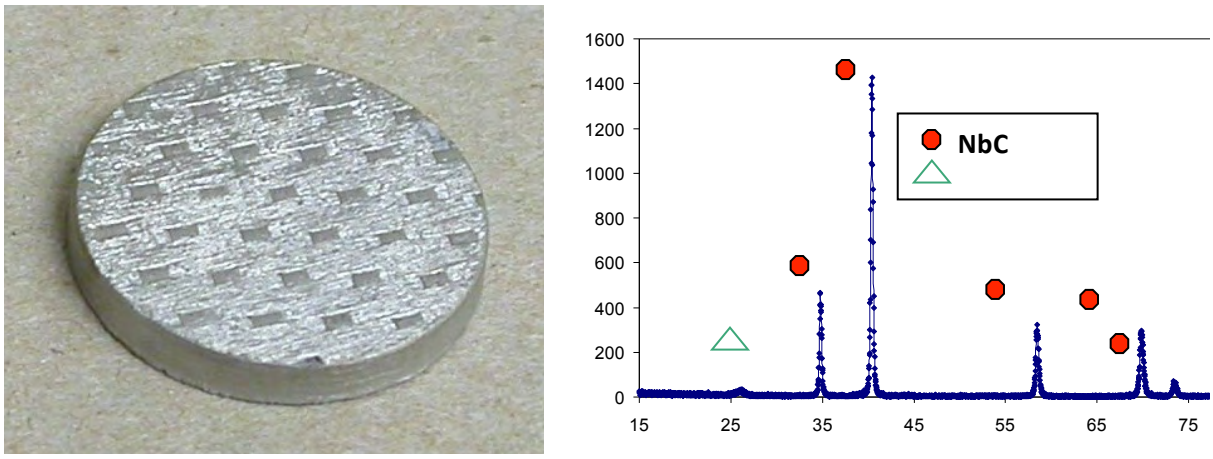

Figure13. Niobium Carbide coating on carbon/carbon composite using CVT process.

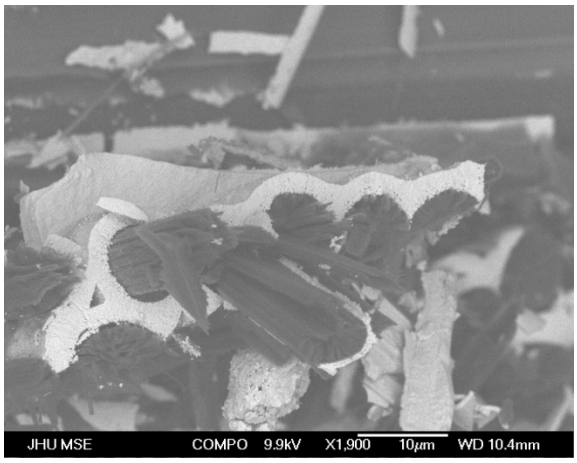

Figure 14 NbC formed on C-C matrix composite.

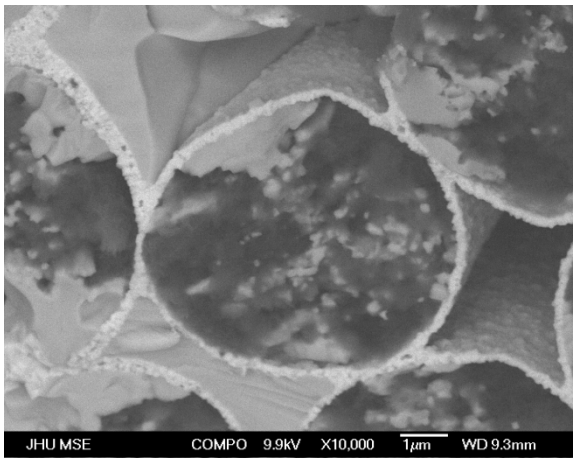

Figure 15 NbC coating on individual carbon fiber surfaces.

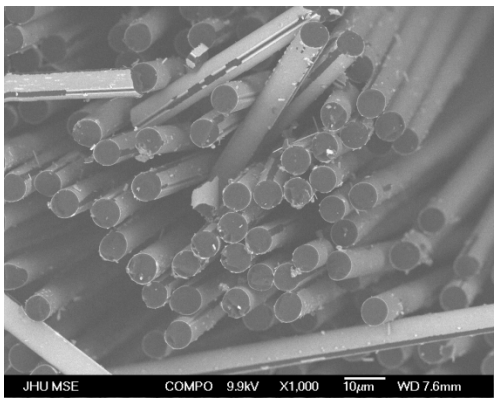

Figure 16(a). ZrC coating formed on individual carbon fibers (cross-section view).

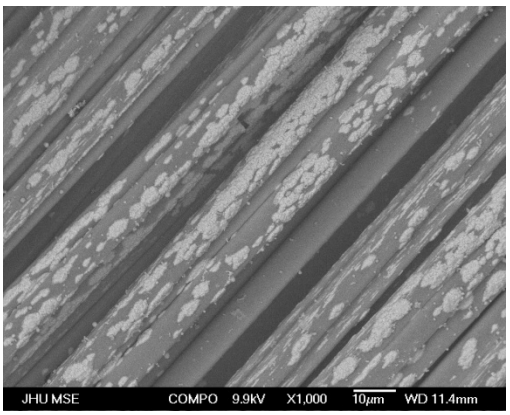

Figure 16(b). ZrC coating formed on individual carbon fibers (side view).

In addition, HfC nanoparticles with an average crystal size under 100nm were also prepared with carbon black nanoparticles as the carbon source (Figure 17) at 900°C. Also shown is the X-ray pattern which shows only the presence of this carbide (Figure 17b). Figure 18 presents the laser particle size analysis of this material. The predominant crystallite size is approximately 100nm. The larger size particles are essentially agglomerates of the 100 nm material.

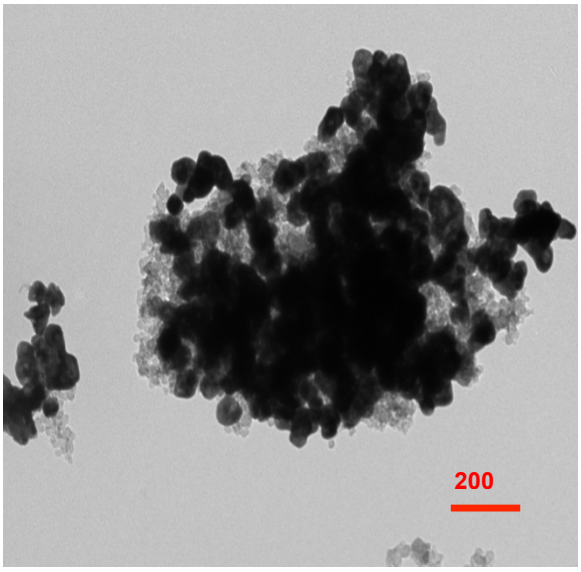

[a]

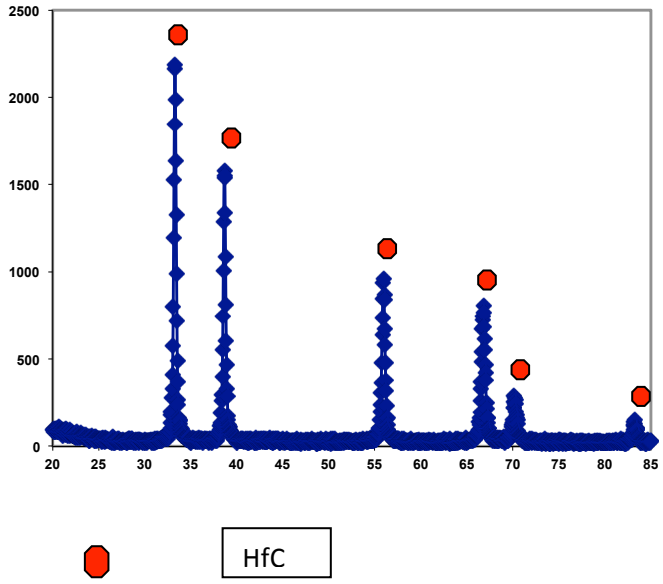

[b]

Figure 17[a] TEM of Hafnium Carbide Nano-Crystals and 17[b] X-Ray diffraction pattern identifying the HfC as the only phase present.

Figure 18 Particle size of Hafnium Carbide Crystals as Measured by a duel wavelength Laser particle size Analyzer

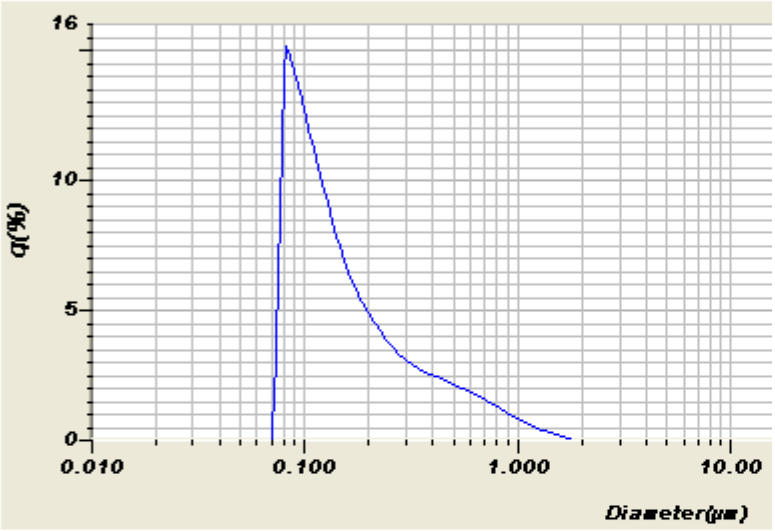

This process has also been used to coat graphite fibers. Figure 19(a) show a SEM of a carbon fiber completely coated with HfC and 19(b) presents a high magnification of the surface coating show that the coating consist HfC crystals ranging from less than 10nm to 100nm. Similar results have been obtained for zirconium, tantalum and vanadium carbides.

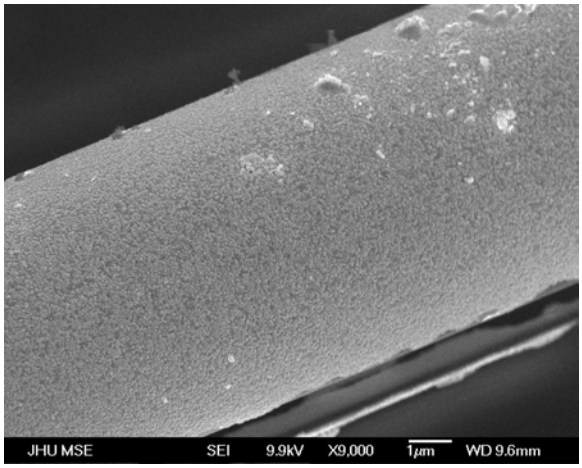

Figure 19a Graphite fiber coated with HfC.

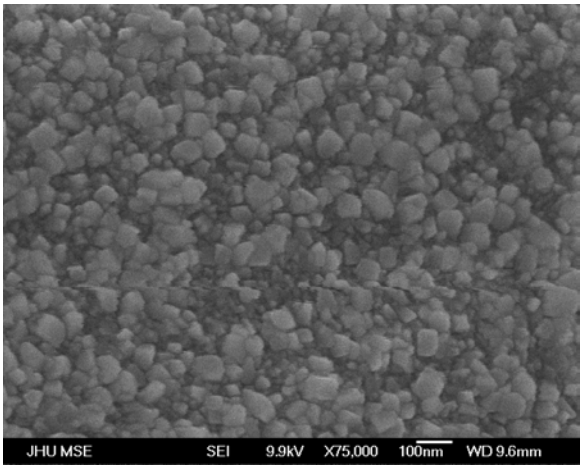

Figure 19b Higher magnification showing Nano-crystalline nature of the carbide coating.

Results shown above have demonstrated that the CVT gas-solid reaction is an excellent technique for forming carbide coatings on both carbon fiber surface and on C-C composites.

Further examination of this technique also suggests that additional improvement was still needed due to the poor adhesion of the carbide coatings, especially for thick coatings. The poor adhesion between the carbon substrate and the carbide coatings is mainly due to two reasons. The first is that during the formation of carbide on the surface of a dense carbon substrate such as carbon fiber with a density of about 1.6 g/cm^3, volume expansion occurs. The degree of volume expansion due to carbide formation on carbon fiber (density 1.6 g/cm^3) for several refractory carbides is shown in Table I. Table I also give the appropriate carbon densities required for the formation of fully dense coatings of these carbides without volume expansion.

Table I. The degree of volume expansion due to carbide formation on carbon fiber (density 1.6 g/cm^3) for several refractory carbides and the appropriate carbon densities required for the formation of fully dense coatings of these carbides without volume expansion.

Carbide	Volume expansion due to carbide formation on carbon with an density of 1.6 g/cm^3	Desirable carbon density for the formation of fully dense carbide without volume expansion (g/cm^3)
ZrC	104.4%	0.866
HfC	108.3%	0.768
TaC	85.1%	0.860
NbC	84.1%	0.841

The second reason for the poor adhesion of carbide coatings on dense carbon is due to the coefficient of thermal expansion (CTE) mismatch between the coating and the substrate. CTE mismatch can be effectively mediated by forming a compositional gradient interface between the carbide and the carbon substrate, and such graded carbide/carbon interface can be generated by using carbon with graded surface density and appropriate surface micro/nano porosity.

It can be concluded that the two factors that affect carbide adhesion as described above can be controlled by using carbon substrates (fibers and composites) with surface of low and graded density. For example, the carbon substrate for ZrC formation should have a density of about 0.866 g/cm^3 at the surface, and the density gradually increases deeper into the inner core, with the thickness of the low density surface layer being tens to a few hundreds of nanometers. Such density graded carbon surface can be achieved either through oxidative surface activation

or application of a low density carbon surface coating. Oxidative surface activation can be carried out by using oxygen plasma, or by partial oxidation in air, water vapor, or carbon dioxide atmospheres. Reaction conditions must be studied in order to control the thickness of the activated layer so the overall structure and mechanical properties are not deteriorated.

5.0 Complete Process for Formation of Chrome Carbide

The following figure illustrates the process path for synthesizing chromium carbide coatings on nickel-based alloys:

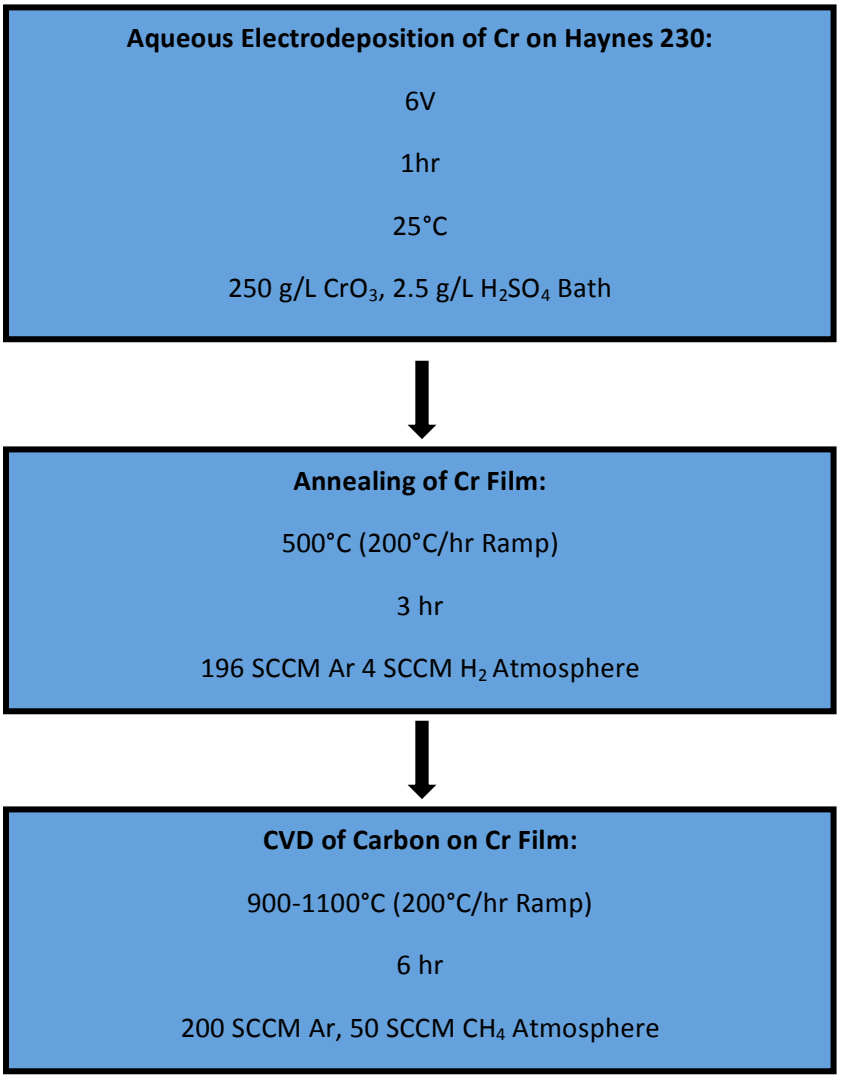

Figure 20: Process Path for Chromium Carbide Synthesis on Haynes 230 Alloy

As the conversion of the chromium film to chromium carbide is accomplished via a gas phase CVD reaction, the inherent porosity of the chromium film is an advantageous microstructural characteristic. It has been noted that two aspects of the CVD process reduce the inherent porosity of the chromium film prior to reaching the CVD process temperature. Annealing of the chromium film at 500°C, which has been implemented in the CVD process path in previous experiments in attempts to promote bonding between the chromium film and the substrate, densifies the chromium film and reduces the inherent porosity of the film prior to reaching the CVD process temperature. The relatively slow ramp rate of 200°C/hr used in previous experiments, which was chosen in attempts to reduce thermal shock of the film, also has the same effect. In order to retain the advantageous as-deposited microstructure of the chromium film, the 500°C anneal was removed from the CVD process and the ramp rate has been changed to the maximum allowable rate of furnace used, 400°C/hr. These changes have shown no detrimental effects on adhesion and improved chromium carbide formation.

As noted above, the initial conversion of chromium films to chromium carbide is facilitated by the inherent porosity of the chromium film. Chromium films subjected to the CVD process at 1100°C showed large amounts of soot formation on the surface of the resulting chromium carbide film. This lends to the notion that the methane decomposition rate at 1100°C likely exceeds the rate at which carbon diffuses into the chromium film grains. As soot builds on the surface of the chromium film in the initial stages of the conversion process the advantageous inherent porosity of the film is negated. For this reason is important to choose a CVD process temperature which minimizes soot formation, but allows for sufficient carbon diffusion rates. A CVD process temperature of 1000°C has shown to be most favorable to the conversion of chromium films to chromium carbide.

Microhardness testing of the chromium carbide films will also be conducted. The proposed molten salt corrosion cell will be fabricated in parallel with the microstructural characterization work outlined above.

5.1 CVD Process Temperature

The following figure illustrates changes made to the apparatus used in the temperature study:

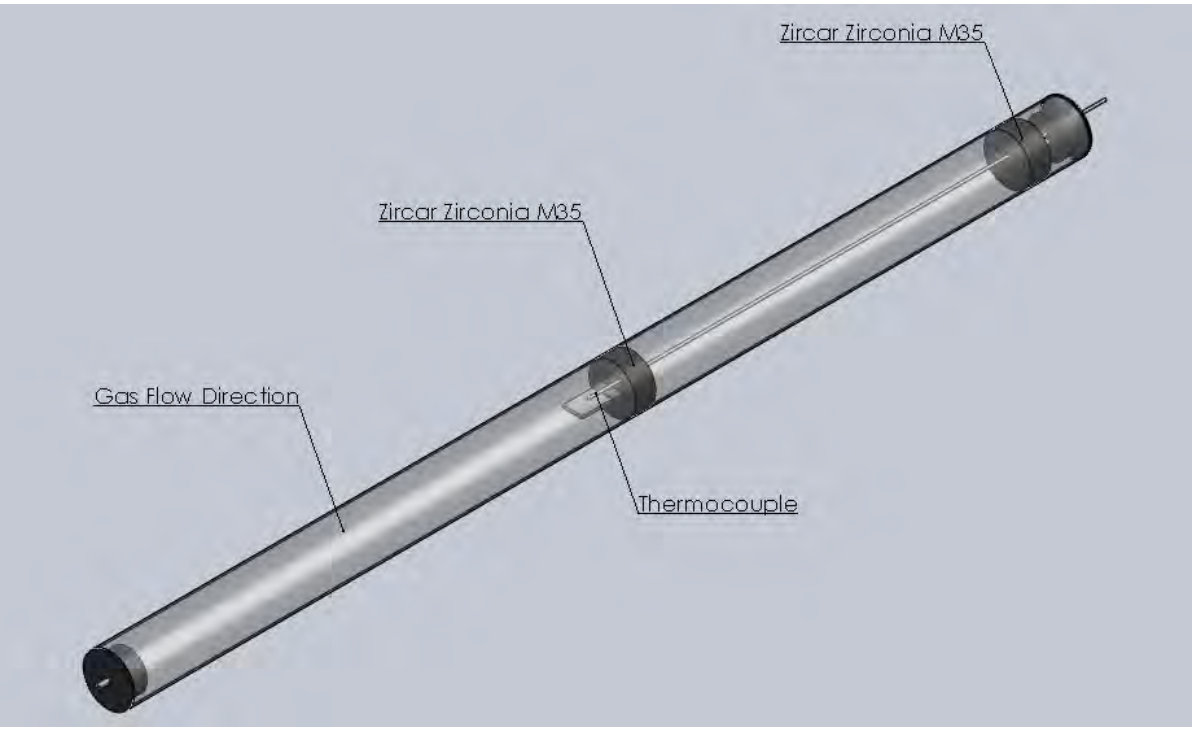

Figure 21: Tube Furnace CVD Apparatus

As shown in Figure 22, a thermocouple is positioned slightly above the sample surface (1/16”). This configuration provides a reasonably accurate measure of the sample surface during the CVD process. Temperature monitoring of the sample surface itself during the CVD process was deemed impractical due to the physical limitations of the apparatus used. Temperature measurements were recorded in LabView at a rate of 1 sample per second. The following plot confirms that the ΔT between the thermocouple used to control the tube furnace and the thermocouple above the sample surface is minimal for chromium films subjected to the CVD process outlined above in the temperature range of 900°C-1000°C:

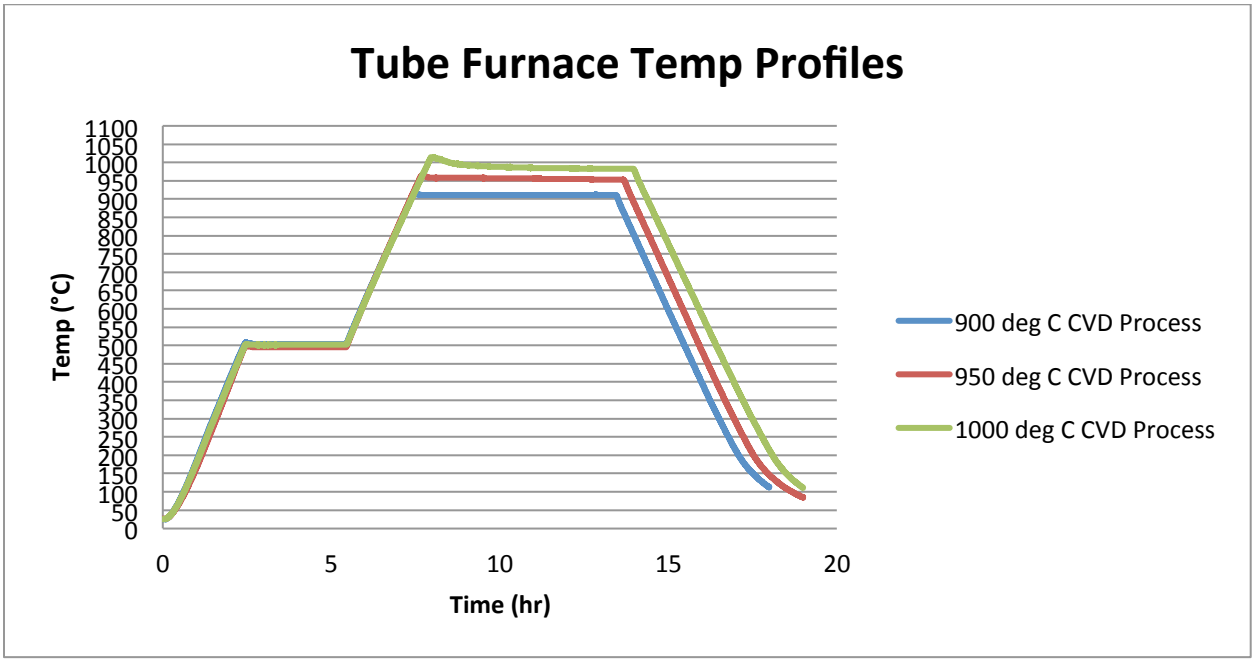

Figure 22: Sample Surface Temperature Measurement

The sample holder and thermocouple support were fabricated from a ceramic board of alumina fibers in a silica matrix. This material was chosen as it is chemically un-reactive to the atmosphere or thermal decomposition in the temperature range studied. The following figure shows the x-ray diffraction results for chromium films subjected to CVD process outlined above in the temperature range of 900°C-1000°C:

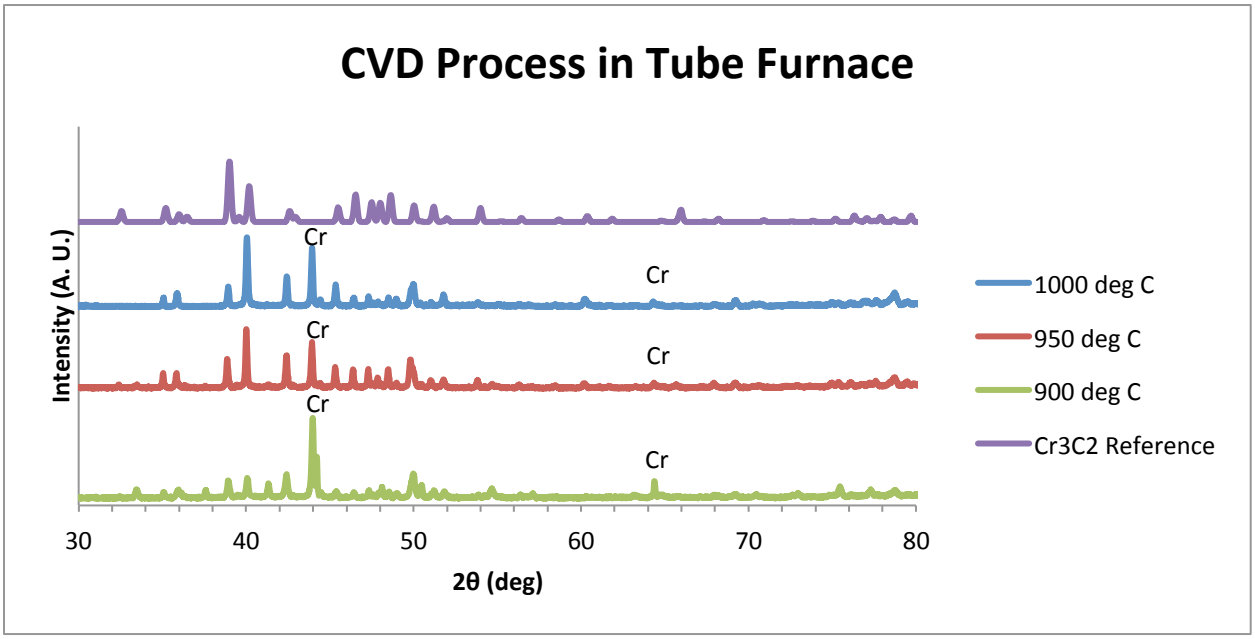

Figure 23: XRD results for chromium films subjected to CVD process in the temperature range of 900°C-1000°C

From the presence of chromium in the x-ray diffraction results shown in Figure 4 it is apparent that the film has not yet been sufficiently converted to chromium carbide. Increasing the reaction temperature decreases the intensity of chromium peaks and increases the intensity of chromium carbide peaks. Further work in the temperature range of 1000°C-1100°C will determine the optimum CVD process temperature.

5.2 CVD Process in Retort Furnace

An investigation of the ability to scale up the CVD process in order to account for multiple samples and various sample geometries was conducted in an Inconel retort furnace. The following figure illustrates the configuration of the temperature monitoring system used in the Inconel retort furnace:

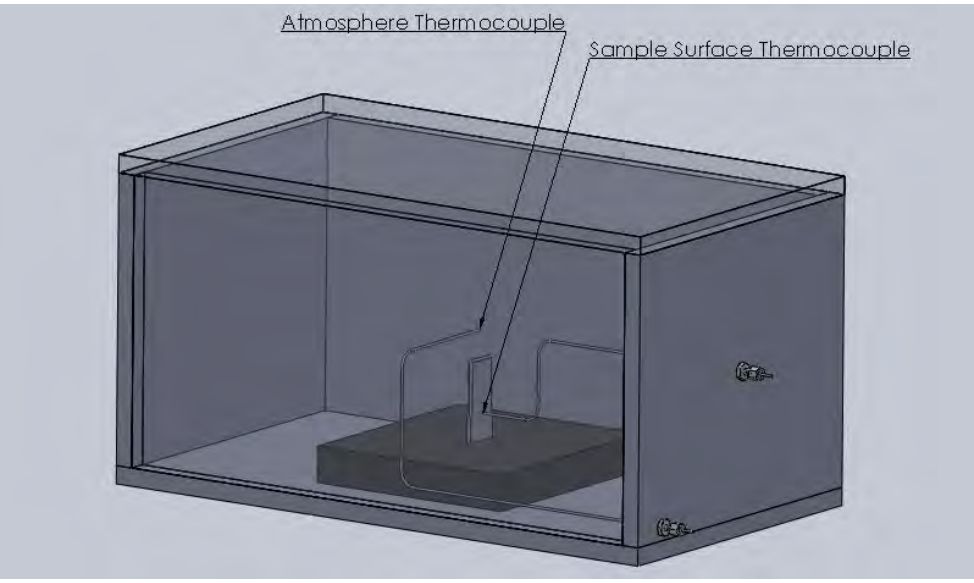

Figure 24: Inconel Retort CVD Apparatus

The Inconel retort furnace allowed for direct measurement of the sample surface temperature during the CVD process, as opposed to the configuration discussed above for the tube furnace. The temperature of the surrounding atmosphere was also measured and recorded via LabView. A graphite block was fabricated as a sample holder as it is unreactive to the atmosphere used in the CVD process

6.0 Conversion of Chromium Oxide to Chromium Carbide

The mechanisms and the kinetics of the reduction of chromium oxide (Cr_2O_3) powder and pressed pellets with methane-containing gas have been studied extensively and the body of related work is a testament to the industrial importance of this process [1-5]. Although the details of proposed mechanisms describing reduction vary, one central notion prevails – namely,

a particular phase of chromium carbide, Cr_3C_2, is the end product of complete conversion. Also, there is agreement on the pronounced effect that methane concentration has on the rate of reduction – above a critical methane concentration the deposition of carbon can strongly retard Cr_3C_2 formation. In addition, the relatively low temperatures and short reaction times observed by many authors for complete conversion to Cr_3C_2 compared to solid-state carbothermal reduction processing [6,7] highlight the usefulness of exploiting a vapor-phase reducing agent. Beyond the production of Cr_3C_2, this material plays a significant role as a component in feedstock powder for cermet thermal spray coatings.

In order to facilitate bonding between the feedstock powder and the substrate during spraying, a metallic binder phase (e.g. NiCr) is used for the deposition of Cr_3C_2 via thermal spray techniques such as high velocity oxy-fuel (HVOF). Significant effort examining the behavior of HVOF Cr_3C_2-NiCr cermet coatings in diverse end-use conditions has shown that the functionalities of these coatings are heavily influenced by the presence of the NiCr binder phase [8-10]. For example, for erosion performance, one of two erosion mechanisms predominately affected the NiCr binder phase in turn degrading coating integrity [8]. Similarly, hot corrosion in molten oxide salt environments was limited by oxidation of the NiCr binder phase [9]. For tribology applications, the size and the distribution of Cr_3C_2 particles within the NiCr binder phase affected the abrasive wear resistance, suggesting that variations in cohesion between these differing materials contributed to the measured wear rate fluctuations [10]. These characteristics of HVOF Cr_3C_2-NiCr cermet coatings and the deposition requirements for Cr_3C_2 suggest that a carbide coating formation process which takes advantage of thermal spray technologies without requiring the use of a NiCr binder phase could produce coatings with improved performance for a range of applications.

Even though there are many studies concerning the reduction of Cr_2O_3 powder and pressed pellets with methane-containing gas, the synthesis of binder-free Cr_3C_2 coatings via reduction of thermally-sprayed Cr_2O_3 appears to be relatively unexplored. In this work, the reduction of atmospheric-plasma-sprayed (APS) Cr_2O_3 with methane-containing gas has been investigated. Plasma-sprayed Cr_2O_3 coatings were exposed to a flowing, methane-containing atmosphere at 1000 ºC to isothermally convert the as-deposited oxide to Cr_3C_2. Mechanisms of reduction as well as the minimum reaction times required for complete conversion to Cr_3C_2 were investigated using microstructural characterization throughout the reduction process.

Measurements were carried out using X-ray diffraction (XRD) and scanning electron microscopy (SEM) to determine phase morphology and porosity evolution in the coating.

6.1 Substrate materials and preparation

Due to the temperature range of interest for Cr_2O_3 reduction experiments which exploit methane-containing gas as a reducing agent (800-1200 ºC) [1-5], substrate materials are generally limited to those capable of undergoing short-term, high-temperature exposure without incurring considerable microstructural re-arrangement. These materials include advanced ceramics (e.g. carbon fiber-reinforced carbon) and Ni-based alloys commonly used in high-temperature applications. Since carbon-based materials could act as a supplementary solid-state source of carbon for Cr_2O_3 reduction, a Ni-based alloy substrate was selected for this study – Haynes 230 (H230). The nominal chemical composition of this alloy is shown in Table 1 [11].

Table 2. Nominal Chemical Composition (wt. %) of H230 alloy.

Ni	Cr	W	Mo	Fe	Co	Mn	Si	Al	C	La	B
57	22	14	2	3	5	0.5	0.4	0.3	0.10	0.02	0.015

Coupons measuring 76.2 x 25.4 x 3.175 mm were machined from a H230 sheet (per AMS 5878 rev. C) using waterjet cutting. Surface preparations for plasma spraying involved grit blasting with 36 grit Al_2O_3, followed by cleaning with isopropyl alcohol and compressed air in an effort to remove adherent oxide particles.

6.3 Cr_2O_3 coating deposition

The deposition of Cr_2O_3 by means of APS does not require the use of a metallic binder phase (as is the case of thermally-sprayed Cr_3C_2), but a bond layer is typically applied between ceramic deposits and metallic substrates to reduce thermal-mismatch stresses that can occur in high-temperature applications. In this work, a NiCr-Al bond layer between the Cr_2O_3 top coat and the H230 substrate was used to moderate cracking and spallation of the oxide coating during

heating to the reduction temperature (1000 ºC). SEM micrographs of the feedstock powders used in this work are shown in Fig. 25 and their characteristics are provided in Table 2.

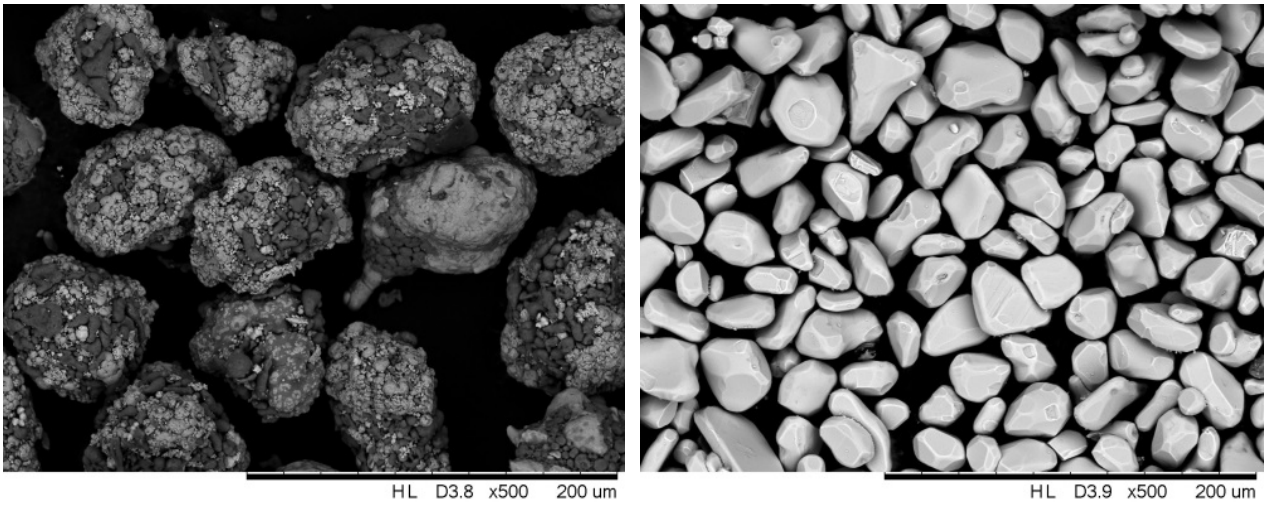

(a) **(b)**

Figure 25 SEM micrographs of feedstock powder morphologies: (a) NiCr-Al used in the bond layer and (b) Cr_2O_3 used in the top coat.

Table 3. Plasma Spray Powder Feedstock Powder Characteristics.

Feedstock Powder	Chemical Composition (wt. %)	Particle Size (μm)	Morphology
Metco 443NS (NiCr-Al)	Ni 18.5Cr 6Al	-125 +45	Spherical
Amdry 6420 (Cr_2O_3)	99.5+ Cr_2O_3	-45 +22	Irregular

An APS system consisting of a Metco 9MB plasma gun, Bay State Surface Technologies Model 1200 powder feeder and Yaskawa Motoman HP20 robot movement was used for the deposition of both the NiCr-Al bond layer and the Cr_2O_3 top coat. APS deposition conditions are reported in Table 3.

Table 4 Atmospheric Plasma Spray (APS) Deposition Conditions.

Feedstock Powder	Voltage (V)	Current (A)	Working Distance (mm)	Traverse Speed (mm/s)	Step Size (mm)
Metco 443NS	75	500	127	416.56	3.175
Amdry 6420	70	500	69.85	416.56	3.175

6.4 Reduction of plasma-sprayed Cr_2O_3 with methane-containing gas

Plasma-sprayed Cr_2O_3 coatings were exposed to a flowing, methane-containing atmosphere (80 vol. % Ar with 20 vol. % CH_4; 250 SCCM) in a horizontal quartz tube (60 x 64 x 1300 mm) furnace for 0.1-0.3 h at 1000 °C. The system was purged for 3 h with 400 SCCM Ar prior to the initiation of the thermal cycle. Heating and cooling ramps were carried out at a rate of 400 °C/h and 200 °C/h respectively, with an atmosphere of 200 SCCM Ar. Ultra-high purity gas sources were used in conjunction with an in-line purifier (Matheson Nanochem Purifilter) to further reduce O_2 and H_2O impurity levels (<0.1 ppb O_2 and H_2O). The gas mixture composition was regulated through the use of mass flow controllers (Alicat Scientific Series MC) [12].

6.5 Microstructural characterization

The coating phase evolution throughout the reduction process was determined using X-ray diffraction with a Philips X'Pert Pro Materials Research Diffractometer equipped with a Cu-Kα source. A programmable divergence slit was used to the hold irradiated length constant (8 mm) throughout the scan range thereby increasing the signal-to-noise ratio for high-angle diffraction peaks.

Phase morphology and porosity evolution were examined in coating cross sections for various reduction times (0.1-0.3 h) with a Hitachi TM3000 tabletop SEM. Samples were initially vacuum-impregnated with Buehler EpoThin low-viscosity epoxy at a pressure of 33.6 kPa. Sectioning, grinding and polishing were then performed using the recommended techniques for the metallographic preparation of thermally-sprayed ceramics [13]. A Buehler IsoMet 1000 low-speed precision diamond saw and a Buehler EcoMet 3000/AutoMet 2000 semi-automatic grinder/polisher were used for sectioning and grinding/polishing respectively.

6.6 Characterization of Cr_2O_3 Conversion to Carbide

Aspects of the Cr_2O_3 reduction process are directly related to the characteristics of the as-deposited coating microstructure. XRD measurements of the Cr_2O_3 feedstock powder and the resulting plasma-sprayed coating (Fig. 26) indicate no appreciable compositional changes as a

result of the deposition process. Although thicker coatings were employed for reduction experiments, the SEM cross-sectional micrograph shown in Fig.27 is representative of the plasma-sprayed Cr_2O_3 used in this work. The as-deposited coating microstructure contains globular voids and interlamellar porosity which are characteristic of a wide range of thermally-sprayed materials [14] as well as the intralamellar microcracks that occur in brittle ceramics [15].

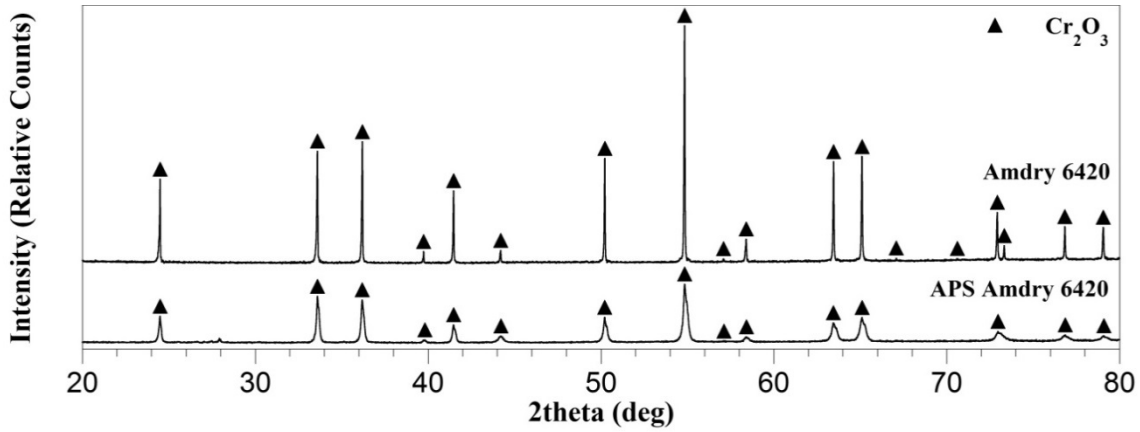

Fig. 26. XRD patterns of the Cr_2O_3 feedstock powder used in this work (top scan) and the resulting plasma-sprayed coating (bottom scan), indicating no appreciable compositional changes as a result of the deposition process.

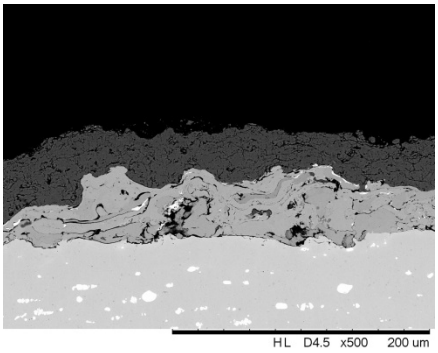

Fig. 27. Cross-sectional SEM micrograph of plasma-sprayed Cr_2O_3 (top coat), showing a complex pore structure containing globular voids, interlamellar porosity and intralamellar microcracks.

Despite uncertainty regarding the mechanism of reduction of Cr_2O_3 powder and pressed pellets with methane-containing gas, there is agreement that the conversion to Cr_3C_2 largely proceeds by the following overall reaction [1-5]:

$$3Cr_2O_{3(s)} + 13CH_{4(g)} \rightarrow 2Cr_3C_{2(s)} + 9CO_{(g)} + 26H_{2(g)} \quad (1)$$

In this work, it was found that the complete conversion of plasma-sprayed Cr_2O_3 to Cr_3C_2 occurred over timescales similar to those reported in related work which exploited vapor-phase reducing agents [1-5], but differed significantly from those reported for solid-state carbothermal reduction investigations [6,7]. The XRD patterns in Fig. 28 show the coating phase evolution for reduction times of 0.1-0.3 h at 1000 ºC.

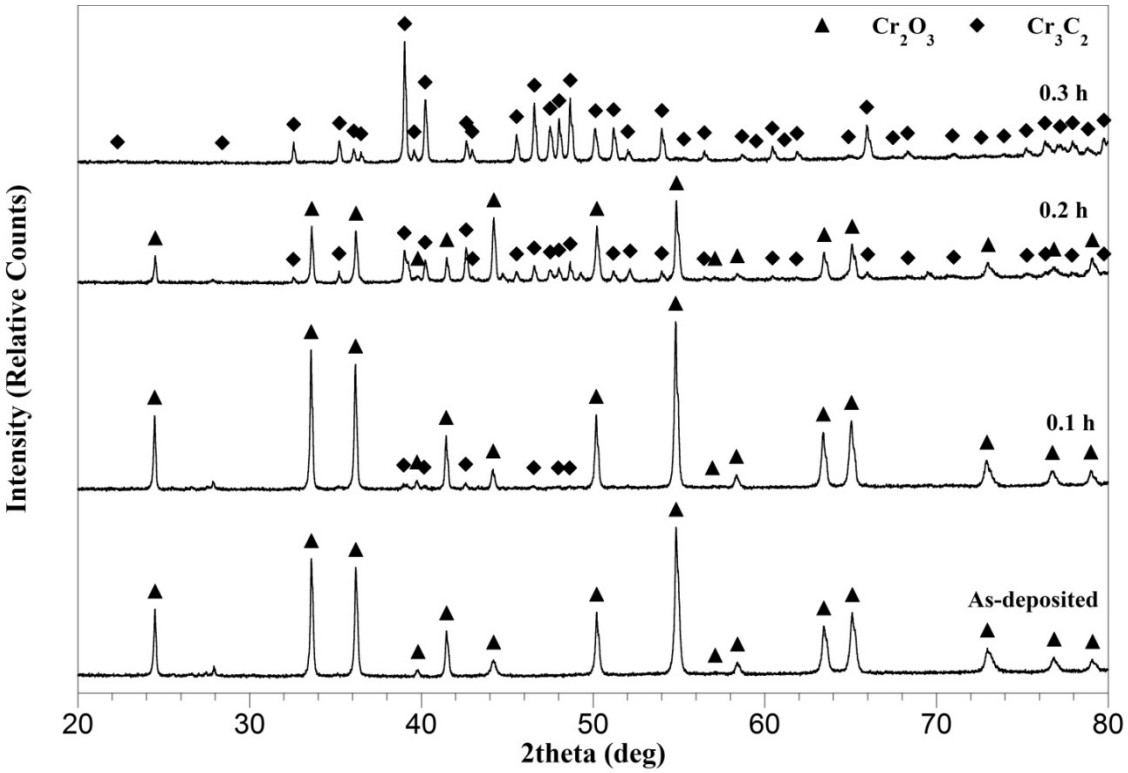

Figure 28 XRD patterns of plasma-sprayed Cr_2O_3 after various reduction times (0.1-0.3 h) at 1000ºC, showing coating phase evolution from Cr_2O_3 to binder-free Cr_3C_2.

For a reduction time of 0.1 h, the onset of Cr_3C_2 formation is observable while Cr_2O_3 clearly remains the major phase in the coating. With increased reduction time (0.2 h), it is apparent a substantial volume fraction of the Cr_2O_3 coating is converted to Cr_3C_2. After 0.3 h, the conversion to Cr_3C_2 is complete (to the penetration depth of the X-ray beam), and an XRD pattern with relative intensities closely matching randomly oriented, polycrystalline Cr_3C_2 is achieved [16]. These measurements demonstrate the ability to form binder-free Cr_3C_2 coatings via reduction of plasma-sprayed Cr_2O_3 with methane-containing gas – this is one of the principal results of this work. Previous investigation has shown the initial porosity in sprayed Cr coatings

affects the carburization process [17], and it is conceivable that defects in plasma-sprayed Cr_2O_3 could serve a similar role in achieving through-thickness conversion. The SEM micrographs in Fig. 29 show the coating phase morphology and porosity evolution throughout the reduction process, and illustrate characteristics of the mechanism of reduction with methane-containing gas when employing a plasma-sprayed coating precursor.

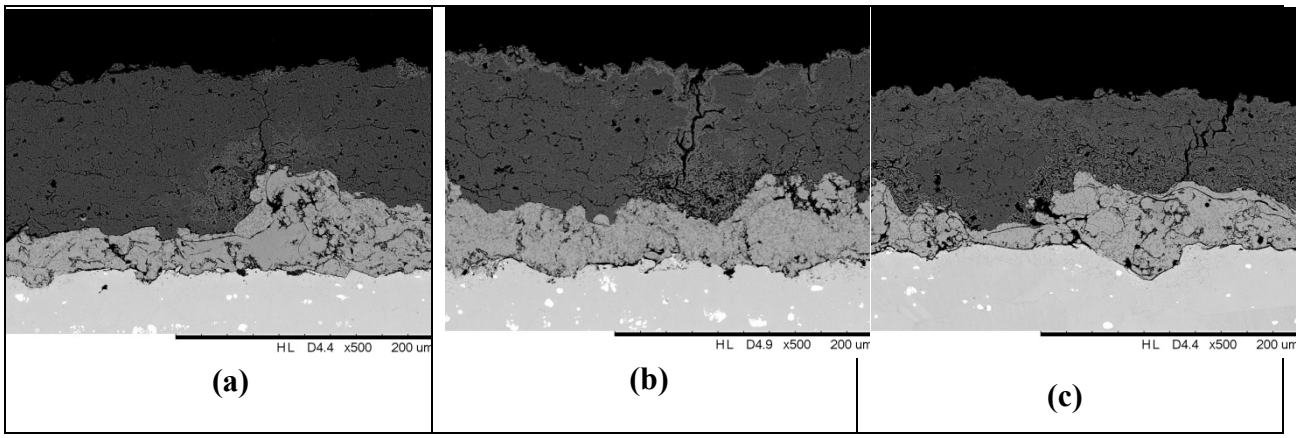

Fig. 29. Cross-sectional SEM micrographs of plasma-sprayed Cr_2O_3 after various reduction times at 1000ºC, illustrating characteristics of the mechanism of reduction to binder-free Cr_3C_2: (a) 0.1 h, (b) 0.2 h, (c) 0.3 h.

At the earliest reduction time (0.1 h) the onset of Cr_3C_2 formation (visible in areas of increased image brightness relative to the surrounding unconverted Cr_2O_3) appears to be limited to the near-surface region of the coating and to areas containing sizeable microcracks oriented normal to the plane of the coating (Fig. 29a). Considering that the out-of-plane dimensions of these microcracks far exceed splat thicknesses and also that they were not present in the as-deposited Cr_2O_3 coating microstructure (Fig. 27), it is likely they result from thermal-mismatch stresses generated by heating to the reduction temperature (1000ºC) [14,15]. Even though the NiCr-Al bond layer did not prevent microcracking, the enhanced rate of reduction in the vicinity of microcracks indicates that defects in plasma-sprayed Cr_2O_3 facilitate through-thickness conversion. Inspection of Fig. 29b for a reduction time of 0.2 h further suggests that multiple pathways for reduction are acting. While reduction seems to proceed in-plane by means of thermal-stress-generated microcracks, carbide formation also occurs progressively from the surface to underlying unconverted Cr_2O_3 in other regions of the coating microstructure.

Although the imaging results for a reduction time of 0.3 h (Fig. 29c) agree with the XRD measurements presented in Fig. 28 (the Cr_3C_2 surface layer thickness exceeds the X-ray beam penetration depth) an underlying portion of oxide remains unconverted in regions of increased Cr_2O_3 thickness. In areas of the microstructure containing thermal-stress-generated microcracks, carbide formation has progressed through the coating thickness. Closer examination of the interface between the Cr_3C_2 surface layer and the underlying unconverted Cr_2O_3 in Fig. 29c reveals a significant difference in porosity between the two phases (Fig. 6). Void formation of similar character has been documented in previous work involving the conversion of Cr_2O_3 powder to Cr_3C_2 via reduction with methane-containing gas [27]; however, in this particular instance it is probable that the newly-formed microporous Cr_3C_2 is a combined result of the constraint on coating dimensions imposed by the substrate and the specific volume decrease associated with Eq. 1 (38.1 %). Irrespective of the coating location under consideration, a thick, continuous surface layer of adherent, binder-free Cr_3C_2 is formed after a reduction time of 0.3 h.

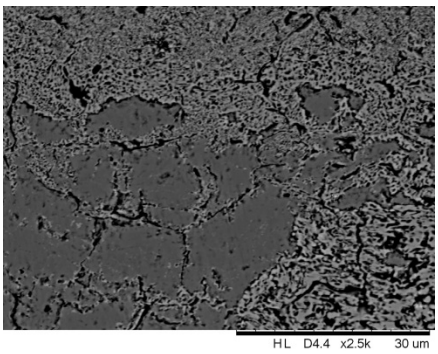

Fig. 30. Void formation in the Cr_3C_2 phase formed from the reduction of plasma-sprayed Cr_2O_3. Label "A" corresponds to unconverted Cr_2O_3 and label "B" corresponds to newly-formed microporous Cr_3C_2.

6.7 Discussion of Conversion of Chromium Oxide to Carbide

Although thermogravimetric or on-line off-gas mass spectroscopy techniques will be needed to quantify the reaction kinetics of the reduction of plasma-sprayed Cr_2O_3 with methane-containing gas [27,28,31], a qualitative understanding can be gained from the XRD and SEM results presented in Figs. 4 and 5. Since non-catalytic gas-solid reactions are inherently multi-

step phenomena, both chemical and physical (diffusional) processes must be considered when identifying the rate-limiting step in the overall reaction [43, 44]. The lack of diffraction peaks belonging to carbon in the XRD patterns for all of the reduction times in this work (Fig. 33) suggests the newly-formed microporous Cr_3C_2 is a non-catalytic surface for methane decomposition. Also, this lack of carbon deposition indicates that the diffusion of reducing agents rather than their chemical reactivity is probably the rate-limiting step in the overall reduction reaction. This notion contrasts with previous modeling involving the overall reaction kinetics of the reduction of pressed Cr_2O_3 pellets with methane-containing gas [28] which operated under the assumption that chemical reactivity was the rate-limiting step. However, the low-density pressed pellets were formed from an initially porous Cr_2O_3 powder of high surface area which likely resulted in a physical system that supported such a model. Regardless of the rate-limiting step under consideration, the progression of conversion over time (Fig. 5) seems to indicate that the overall reduction reaction extent is non-linear in nature when employing a plasma-sprayed Cr_2O_3 coating precursor. This is in agreement with previous work using Cr_2O_3 powder and pressed pellets which quantified overall reduction reaction extent under isothermal conditions using various techniques [27, 31]. In addition, the timescale over which complete conversion occurs (less than 0.5 h) compares favorably with these previous reports – this was unexpected considering the large differences in density between the powder, pressed pellet and plasma-sprayed Cr_2O_3 preforms.

Also of significance is the disparity between the timescales required for the complete conversion of plasma-sprayed Cr and Cr_2O_3 to Cr_3C_2 under identical conditions. In this work the complete conversion of plasma-sprayed Cr_2O_3 to Cr_3C_2 is realized in less than 0.5 h, whereas previous investigation involving the carburization of plasma-sprayed Cr suggested that complete conversion required at least several hours [42]. A fundamental difference in the mechanism of conversion is probably responsible for this discrepancy. While microcracking in the Cr_2O_3 coating defect structure facilitates rapid through-thickness reducing agent penetration, subsequent transport is likely occurring by means of methane gas diffusion through microporosity in the newly-formed Cr_3C_2 in order to reach unconverted oxide. Specific models will be needed to confirm a self-assisted conversion mechanism of this nature.

The motivation for converting plasma-sprayed Cr_2O_3 to binder-free Cr_3C_2 is related to the behavior of HVOF Cr_3C_2-NiCr cermet coatings in molten oxide salt environments. These cermet

coatings derive their hot corrosion resistance through the development of nickel and chromium oxide scales [35] which are thermodynamically unstable in molten fluoride salts [45]. The ability to form binder-free Cr_3C_2 coatings on nickel-based alloys could be useful for applications requiring corrosion resistance in non-oxide fused salt environments, such as the envisioned use of molten fluoride salts as heat transfer fluids in nuclear reactors [42,46]. While microporosity in the newly-formed Cr_3C_2 might not be beneficial in corrosive environments, the porous Cr_3C_2 surface layer developed in this work could serve as a high hardness and fracture resistant refractory scaffolding for lubricants in high-temperature abrasive wear applications [47].

6.8 Summary of CVD Chromium Oxide Conversion to Chromium Carbide

In this work, a method has been demonstrated for the synthesis of binder-free Cr_3C_2 coatings on nickel-based alloys via the reduction of plasma-sprayed Cr_2O_3 with methane-containing gas. A thick, continuous surface layer of adherent, binder-free Cr_3C_2 has been achieved, with the mechanism of reduction being strongly influenced by the coating defect structure at the reduction temperature. Despite large differences in density between oxide preforms, the conversion of plasma-sprayed Cr_2O_3 to Cr_3C_2 reported here occurs over timescales similar to those in related work which used Cr_2O_3 power and pressed pellets. This might be due in part to the formation of microporosity in the newly-formed Cr_3C_2 which appears to expedite the diffusion of methane gas to unconverted Cr_2O_3. A rigorous and systematic material characterization program will be needed to qualify the binder-free Cr_3C_2 surface layer for potential end-use applications as has been conducted for thermally-sprayed Cr_3C_2-NiCr cermet coatings in recent years.

7.0 Chromium Carbide Coating Formation Process Summary

Previous research that investigated the molten fluoride salt corrosion resistance of nickel-based alloys has pointed towards refractory carbides, and in particular chromium carbides, as candidate materials for corrosion resistant coatings [1]. Although traditional methods such as thermal spray exist for the deposition of chromium carbides (e.g., Cr_3C_2) on industrial-scale components, these techniques require a metallic binder phase (e.g., NiCr) to be sprayed in conjunction with the carbide material for adequate coating adhesion. The presence of a NiCr

binder phase in thermally-sprayed Cr_3C_2-NiCr coatings would present a challenge in studying the intrinsic molten fluoride salt corrosion resistance of Cr_3C_2, as refractory metals such as Cr are selectively attacked by the melt [1]. Accordingly, a novel approach towards the synthesis of binder-free Cr_3C_2 coatings on industrial-scale components has been extensively explored. While several variations of the carbide coating formation process have been considered, each shares the commonality that a Cr-containing coating precursor is converted to binder-free Cr_3C_2 via post-treatment with methane-containing gas. The specific details of each carbide coating formation process variation have been described in manuscripts under various stages of publication. However, a brief summary of the results is provided.

During the early development stages of the carbide coating formation process electrodeposited Cr was used as a Cr-containing coating precursor. This provided a cost-effective means to qualitatively explore a time-temperature-transformation space for the carbide coating formation process, and definitively defined the conversion temperature as 1000 °C for the remainder of the program. Figure 31 shows the X-ray diffraction (XRD) phase evolution of the electrodeposited Cr coating after post-treatment with methane-containing gas for 6 and 12 h at 1000 °C.

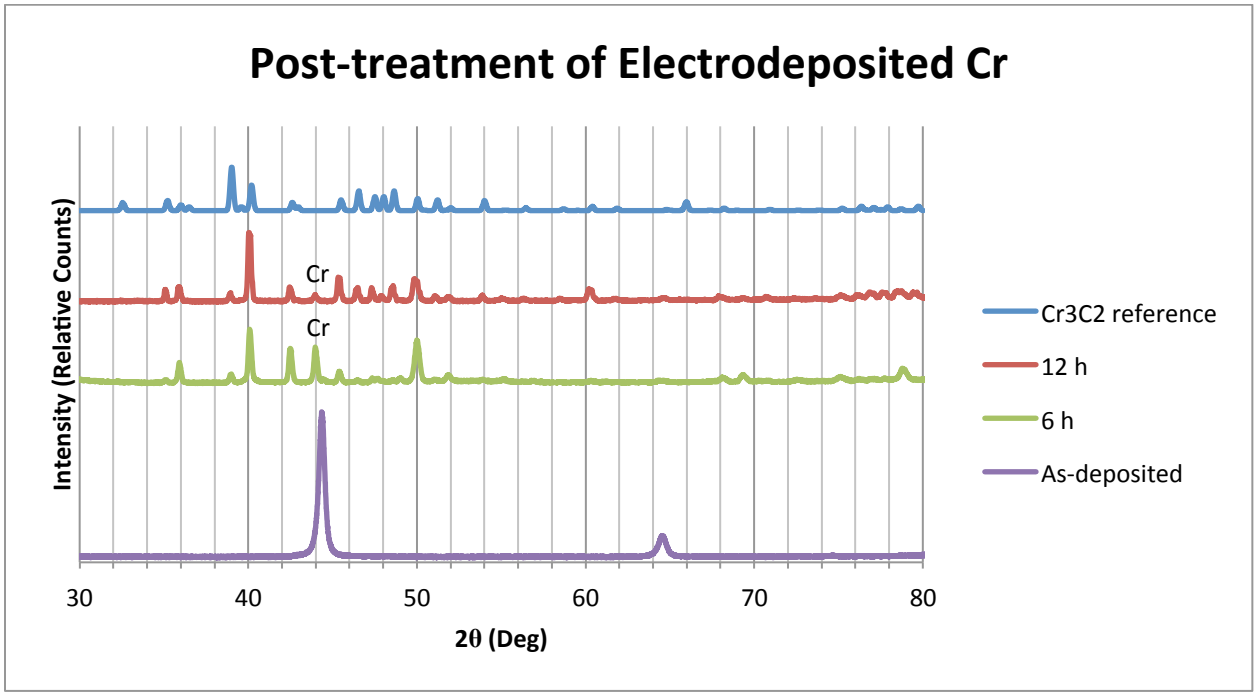

Fig. 31: XRD coating phase evolution of an electrodeposited Cr coating after 6 and 12 h of post-treatment with methane-containing gas at 1000°C.

After 6 h of post-treatment with methane-containing gas it is evident that a significant mass fraction of the coating is converted to Cr_3C_2, while Cr remains as a major phase. An increase of the post-treatment time to 12 h results in near-complete conversion to Cr_3C_2. As the conversion of Cr to Cr_3C_2 is associated with a specific volume increase (23.57 %) and electrodeposited Cr coatings are well known to contain mainly nanoscale porosity, the resultant carbide coating was expected to be sufficiently dense for corrosion applications. For confirmation, scanning electron microscopy (SEM) was used to examine porosity evolution throughout the carbide coating formation process (Fig. 32).

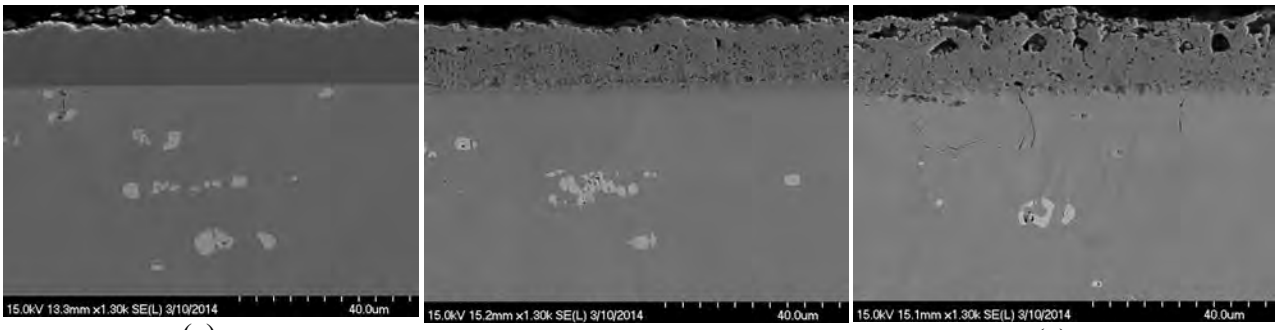

(a) (b) (c)

Fig. 37 SEM micrograph of coating porosity in an (a) electrodeposited Cr coating, (b) electrodeposited Cr coating after 6 of post-treatment with methane-containing gas at 1000 °C and (c) electrodeposited Cr coating after 12 of post-treatment with methane-containing gas at 1000°C.

Intriguingly, the conversion of electrodeposited Cr to Cr_3C_2 results in the development of micron-scale porosity, which is unfavorable for molten fluoride salt corrosion resistance. Due to the relatively thin electrodeposited Cr coating thickness (~ 15 μm) it is unclear whether the micron-scale porosity generation originates from the coalescence of nanoscale voids or as a result of the conversion to carbide.

As a rapid method for depositing Cr-containing coating precursors that are relatively free of nanoscale porosity, plasma spraying was employed. The phase evolution for plasma-sprayed Cr after post-treatment with methane-containing gas for 6 and 12 h is shown in Fig.33.

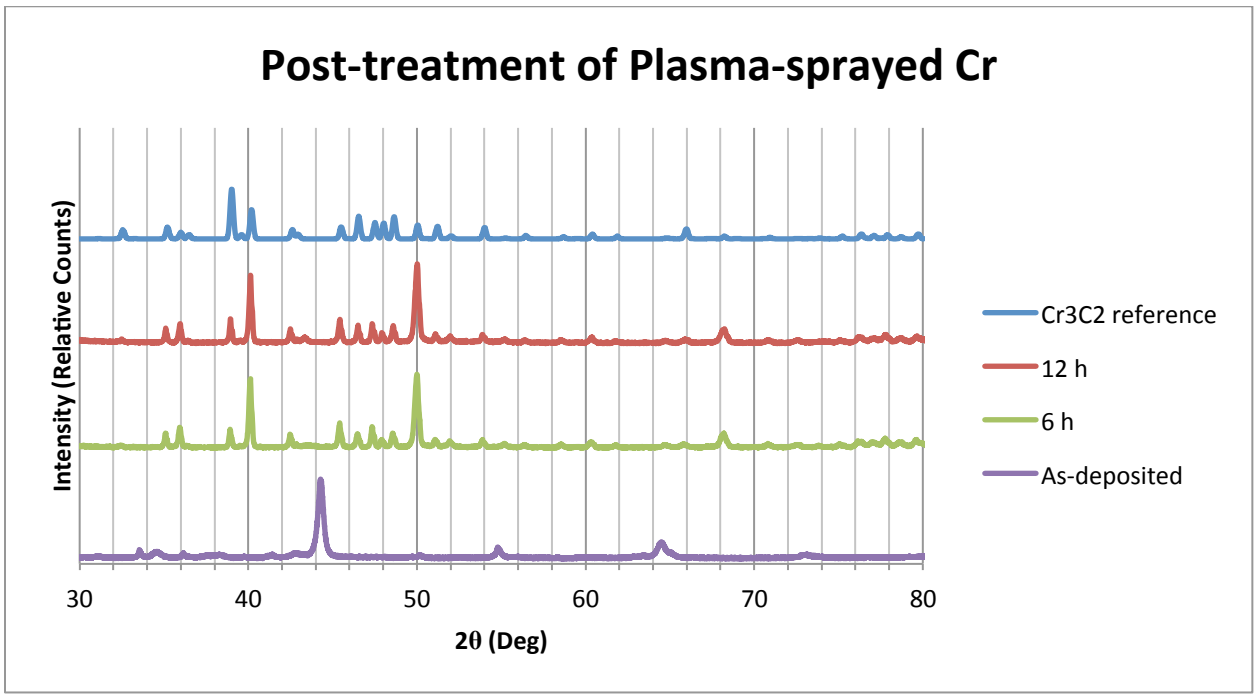

Fig. 33 XRD coating phase evolution of a plasma-sprayed Cr coating after 6 and 12 h of post-treatment with methane-containing gas at 1000 °C.

Interestingly, plasma-sprayed Cr is completely converted to Cr_3C_2 in 6 h or less (Fig. 33), whereas electrodeposited Cr contains a measurable Cr peak even after 12 h of post-treatment with methane-containing gas (Fig. 31). This difference in reaction kinetics may be attributed to the presence of micron-scale porosity in the plasma-sprayed Cr coating, which allows for through-thickness methane gas transport (Fig. 37a). While through-thickness methane gas transport facilitates the conversion to carbide, it prohibits the physical reaction mechanism from being visualized, as the conversion proceeds in all directions. Nonetheless, the conversion of plasma-sprayed Cr to Cr_3C_2 appears to result in an increase in coating porosity (Figs. 34b & 34c), as is the case for electrodeposited Cr (Figs. 32b & 32c).

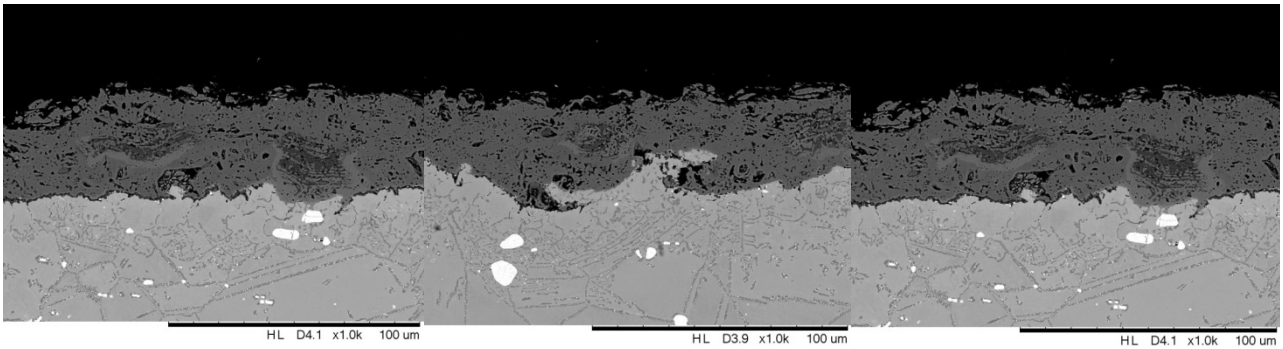

(a) (b) (c)

Fig 34: SEM micrograph of coating porosity in a (a) plasma-sprayed Cr coating, (b) plasma-sprayed Cr coating after 6 of post-treatment with methane-containing gas at 1000°C and (c) plasma-sprayed Cr coating after 12 of post-treatment with methane-containing gas at 1000°C.

In an attempt to identify the physical reaction mechanism governing the seemingly contradictory increase in coating porosity upon conversion to Cr_3C_2, a Cr-containing coating precursor with near theoretical density was needed. Hence, cold spraying was utilized. The reaction kinetics for the conversion of cold-sprayed Cr to Cr_3C_2 are comparable to that of the conversion of electrodeposited Cr to Cr_3C_2, with a measurable portion of the coating remaining as unconverted Cr even after 12 h of post-treatment with methane-containing gas (Fig. 35).

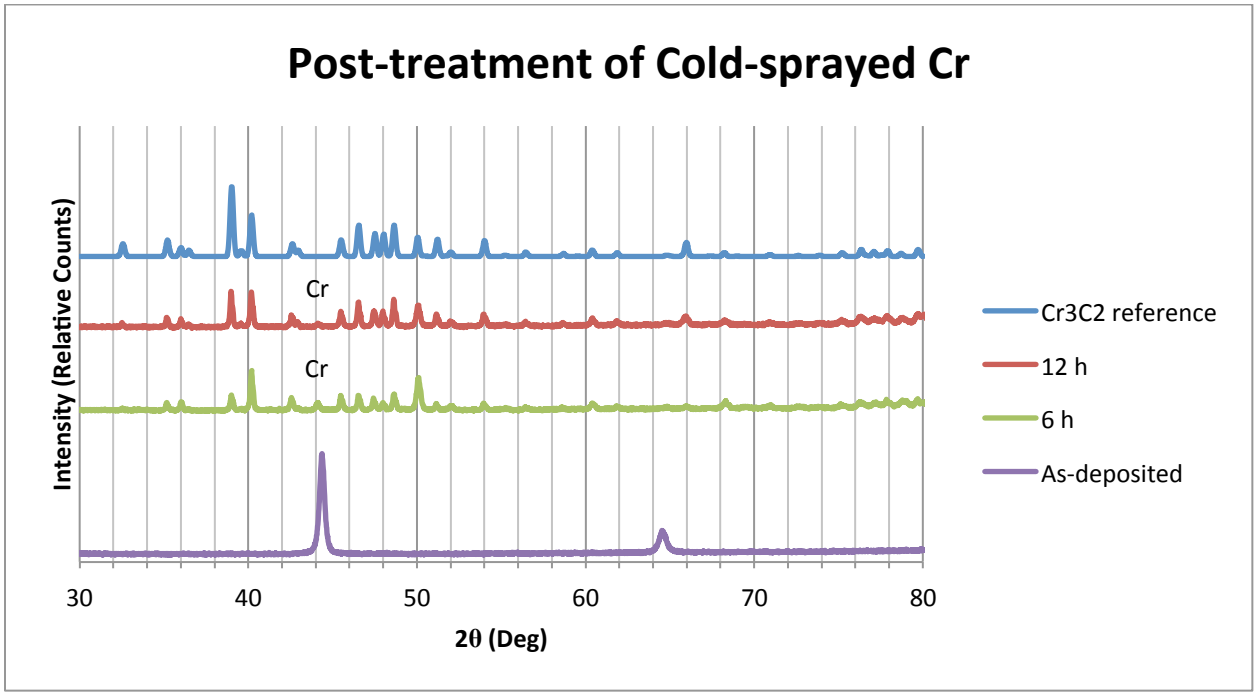

Fig. 35 XRD coating phase evolution of a cold-sprayed Cr coating after 6 and 12 h of post-treatment with methane-containing gas at 1000°C.

Due to a loosely-controlled particle size distribution in the Cr feedstock powders used for cold-spraying, some areas of the cold-sprayed Cr coating contain micron-scale porosity. However, in dense regions the cold-sprayed Cr coating is relatively free of micron and nanoscale porosity (Fig. 36a). Observing the conversion of cold-sprayed Cr to Cr_3C_2 in these dense regions begins to elucidate the physical reaction mechanism at hand. After 6 h of post-treatment with methane-containing gas a band of microporous Cr_3C_2 has emerged at the surface of the coating and a line of micron-scale pores has formed immediately underneath (Fig. 36b). This behavior is suggestive of a physical reaction mechanism that is initially limited by solid-stated diffusion, and is eventually accelerated by the formation of pores in the Cr_3C_2 surface layer (potentially due to

growth stresses), which promotes vapor-phase transport of methane gas to the remaining unconverted Cr.

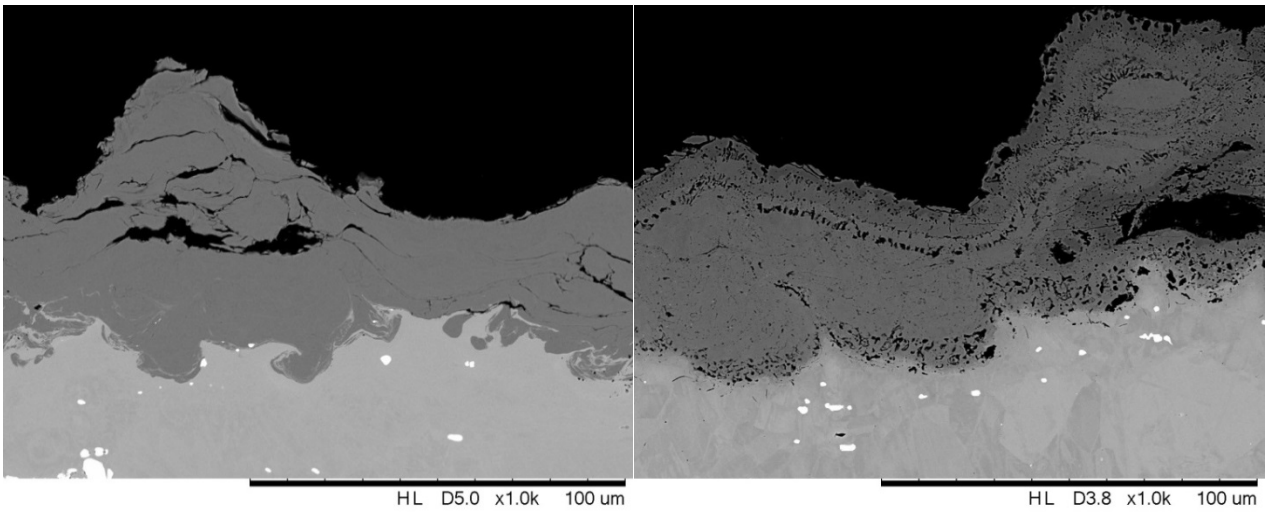

(a) (b)

(c)

Fig.36 SEM micrograph of coating porosity in a (a) cold-sprayed Cr coating, (b) cold-sprayed Cr coating after 6 of post-treatment with methane-containing gas at 1000°C and (c) cold-sprayed Cr coating after 12 of post-treatment with methane-containing gas at 1000°C.

With this physical reaction mechanism in mind, an attempt at expeditiously producing Cr_3C_2 coatings was made by exploiting plasma-sprayed Cr_2O_3 as a Cr-containing coating precursor. Post-treatment of plasma-sprayed Cr_2O_3 with methane-containing gas results in drastically different reaction kinetics compared to what is observed in the instances of electrodeposited Cr, plasma-sprayed Cr and cold-sprayed Cr (Fig. 37).

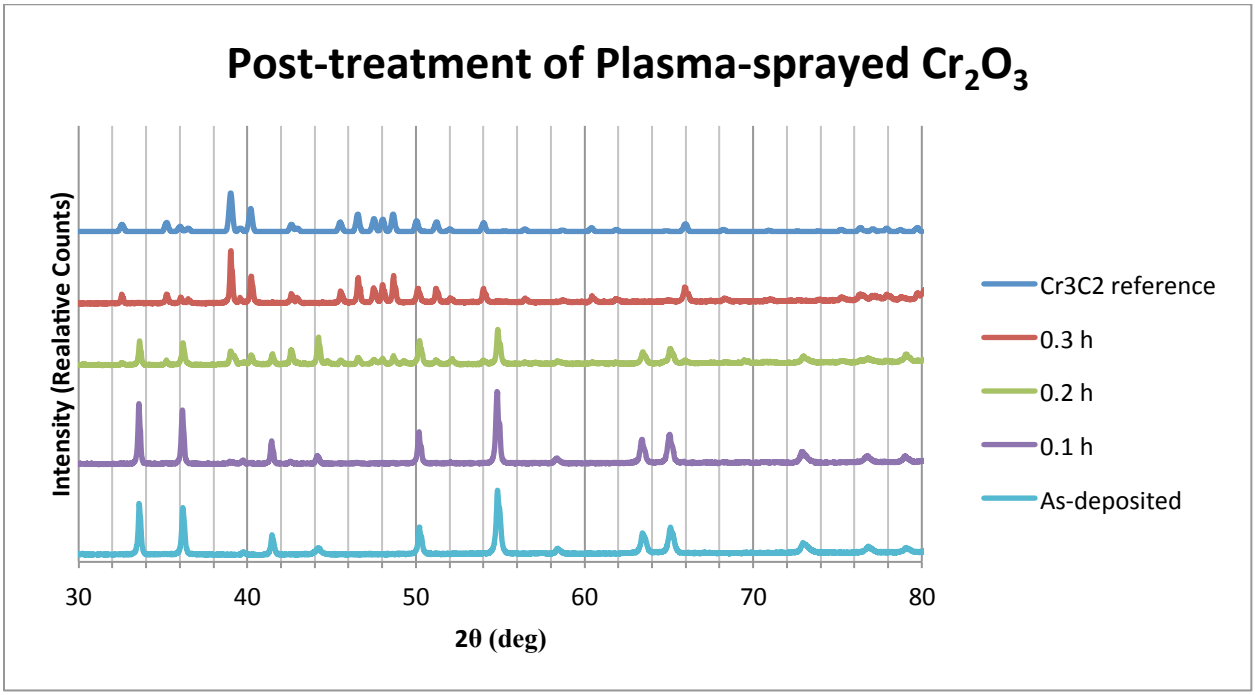

Fig. 37 XRD coating phase evolution of a plasma-sprayed Cr_2O_3 coating after 0.1-0.3 h of post-treatment with methane-containing gas at 1000°C.

After only 0.3 h of post-treatment with methane-containing gas plasma-sprayed Cr_2O_3 is completely converted to Cr_3C_2 (to the penetration depth of the x-ray beam). As the conversion of Cr_2O_3 to Cr_3C_2 is associated with a specific volume decrease (38.10 %), this is likely a result of a physical reaction mechanism with enhanced vapor-phase transport where methane gas can diffuse through a highly-microporous surface layer Cr_3C_2 to unconverted Cr_2O_3 (Fig. 38).

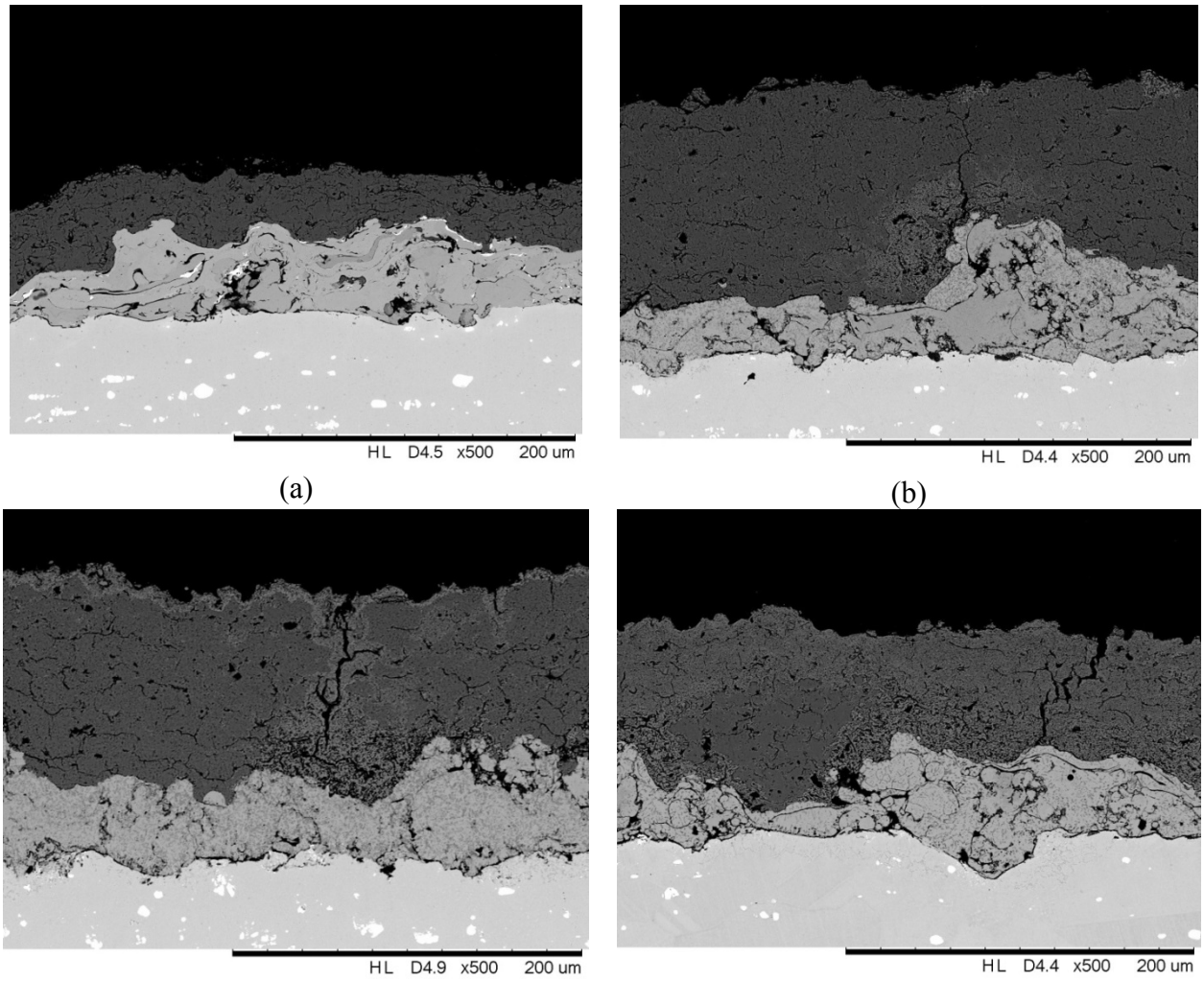

Fig 48: SEM micrograph of coating porosity in a (a) plasma-sprayed Cr_2O_3 coating, (b) plasma-sprayed Cr_2O_3 coating after 0.1 of post-treatment with methane-containing gas at 1000 °C, (c) plasma-sprayed Cr_2O_3 coating after 0.2 of post-treatment with methane-containing gas at 1000 °C and (d) plasma-sprayed Cr_2O_3 coating after 0.3 of post-treatment with methane-containing gas at 1000°C.

Highly-microporous Cr_3C_2 coatings may be useful as refractory scaffoldings for the impregnation of molten fluoride salt corrosion-resistant metals, such Ni or Mo.

Post-treatment of plasma and cold-sprayed Cr with methane-containing gas has resulted in binder-free Cr_3C_2 coatings worthy of further investigation. Therefore, these coatings have been subjected to molten fluoride salt in an attempt to assess the validity of the carbide coating formation process in producing corrosion resistant coatings.

8.0 Molten Fluoride Salt Corrosion Experiment

The design of the molten fluoride salt corrosion experiment is shown in Fig.39.

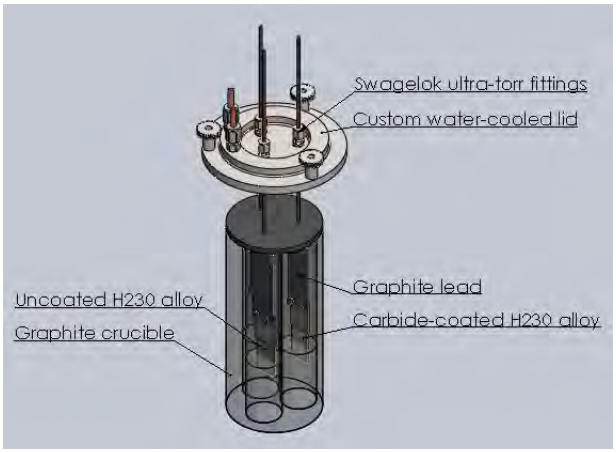

(a)

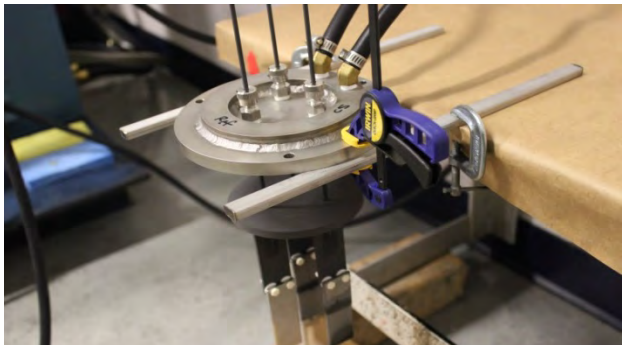

(b)

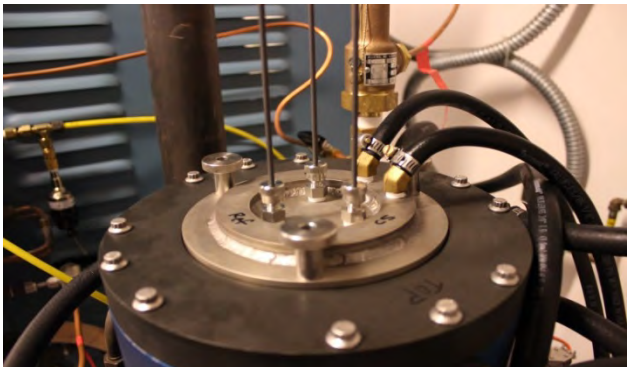

(c)

Fig. 39 (a) Illustration of the molten fluoride salt corrosion experimental design, (b) the fabricated design and (c) the fabricated design loaded into the graphite furnace.

A custom water-cooled lid (fabricated at JHU) allowed for insertion of graphite leads into a graphite furnace through Swagelok Ultra-Torr fittings. These vacuum-rated fittings permitted the graphite leads (and attached uncoated/carbide-coated nickel-based alloys) to be lowered into the molten fluoride salt baths without loss of the furnace atmosphere. The uncoated nickel-based alloy served as a reference material for this experiment. Each uncoated/carbide-coated nickel-based alloy was designed to be suspended in a molten fluoride salt bath within individual graphite crucibles for 500 h at 850 °C under a highly-purified Ar atmosphere. Ultra-high purity Ar flow rate was regulated via mass flow controller and further purified with provisions to strip residual H_2O and O_2 (Fig. 40).

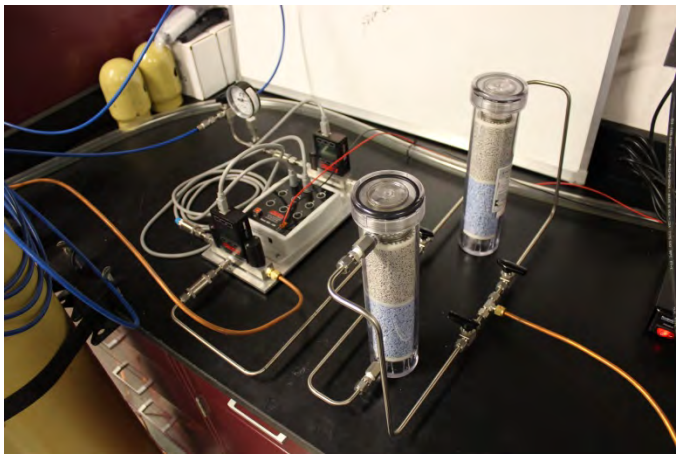

(a)

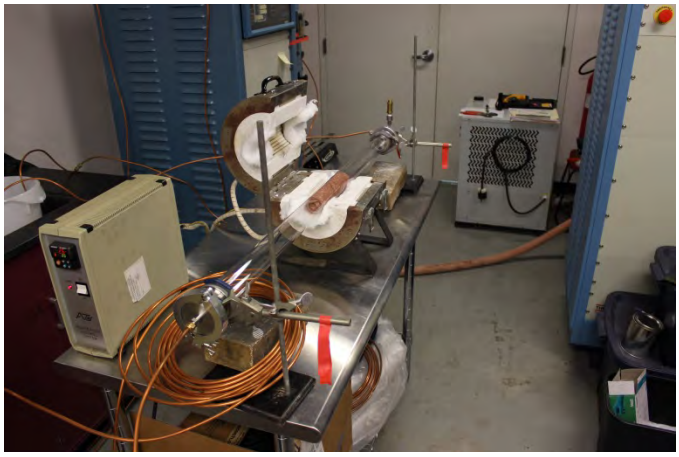

(b)

Fig. 40: Provisions to strip residual (a) H_2O (Drierite desiccant) and (b) O_2 (JHU Cu wool gettering furnace @ 850°C).

In order to provide electrical isolation of samples from one another, alumina nuts/bolts/washers were used between the graphite leads and the uncoated/carbide-coated nickel-based alloys (Fig. 41).

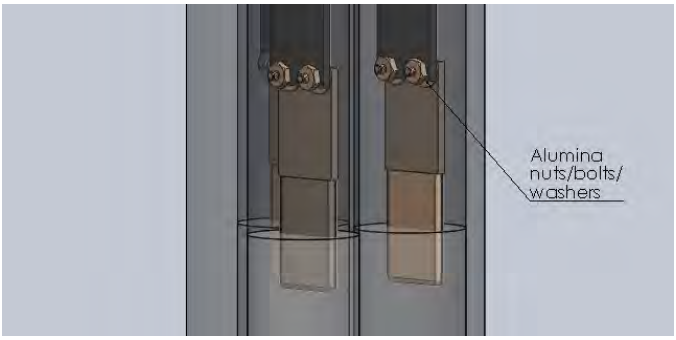

Fig. 41: Illustration of the electrical isolation of samples using alumina nuts/bolts/washers.

All graphite components were custom fabricated (Poco Graphite) and subsequently purified to remove residual machining coolants. A eutectic mixture of LiF-NaF-KF (FLiNaK) subjected to an HF/H_2 sparge purification process (Electrochemical Systems) was used as the molten fluoride salt in this study. The purified FLiNaK was weighed in a glove box with a highly-purified Ar atmosphere (~ 1 ppm H_2O and O_2) and was only briefly exposed to atmospheric contamination during loading of the graphite crucible into the graphite furnace.

Once loaded and sealed, the graphite furnace was immediately evacuated with a roughing pump and held for 12 h @ 300°C to remove any water vapor adsorbed during the transfer process. Ultra-high purity Ar flow was concurrently established through the Cu wool gettering furnace to begin stripping residual H_2O and O_2. Once the graphite furnace began to ramp from 300 °C to 500 °C (melt condition) it was backfilled to atmospheric pressure with highly-purified Ar. The graphite and Cu wool gettering furnace remained under a cover of flowing, highly-purified Ar for the remainder of the experiment. After allowing the molten FLiNaK to homogenize for 1 h at 500 °C the uncoated/carbide-coated nickel-based alloys were lowered into the molten FLiNaK via the graphite leads and Swagelok Ultra-Torr fittings. The graphite furnace was subsequently ramped to 850 °C and set to dwell for 500 h. After dwelling at 850 °C for 232.6 h a fuse blew in the graphite furnace heating circuit and the system cooled to room temperature. Unsure of the origins of the blown fuse, it was replaced and the graphite furnace was ramped back up to 850 °C for what was planned to be the remainder of the dwell. After dwelling at 850 °C for an additional 13.1 h a fuse blew once again. At this point a decision was made to end the experiment after 245.7/500 h of total exposure to FLiNaK at 850 °C. Once the graphite furnace was opened there was no indication of what may have caused the blown fuses, and it is suspected that a failure of the solid-state relay in the graphite furnace heating circuit occurred.

Upon post-exposure inspection of all components a design failure was immediately evident. The alumina nuts/bolts/washers were severely corroded by fluoride salt vapors, causing the uncoated/carbide-coated nickel-based alloys to detach from the graphite leads and become almost entirely submerged in FLiNaK (Fig. 42).

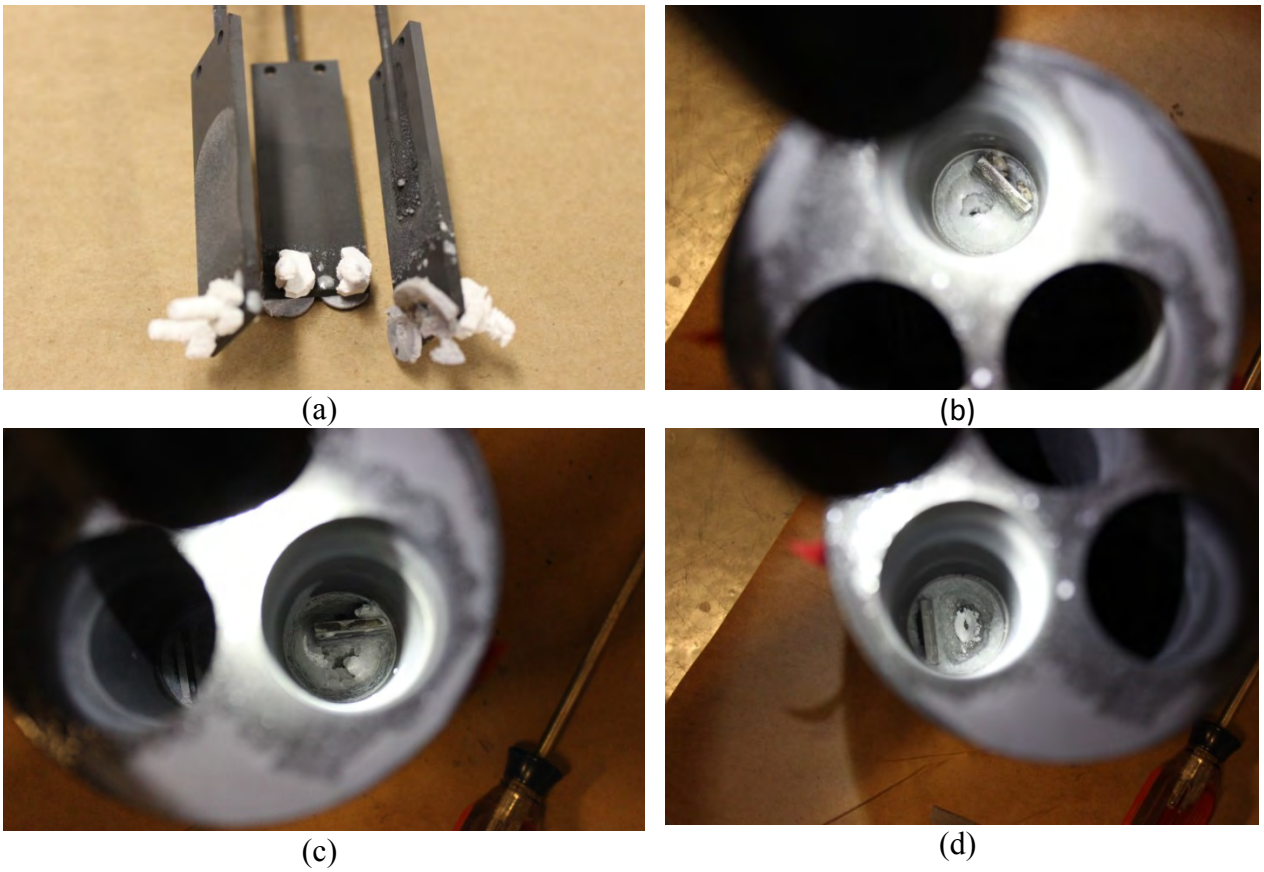

Fig. 42 (a) Extensive corrosion of alumina nuts/bolts/washers by fluoride salt vapor and (b)-(d) detached uncoated/carbide-coated nickel-based alloys nearly submerged in frozen FLiNaK.

While this finding should not invalidate the experiment, it complicates post-exposure salt analysis and the removal of the uncoated/carbide-coated nickel-based alloys from frozen FLiNaK. The final characterization and results of these studies will publish.

9.0 Appendix A Patent Disclosure

9.0 References

1. Ioan Galasiu, Rodica Galasiu, Jomar, Thostad, "Electrochemistry of Molten Salts," in *Nonaqueous Electrochemistry*, edited by Doron Aurbach; Marcel Dekker, Inc.:USA, 1999, pp. 461-591.
2. Process of Forming Metal Ceramic Composites, U.S. Patent No. 4,710,348, Dec. 1987, John M. Brupbacher, Leontios Christodoulou, and Dennis C. Nagle.
3. S.H. White, U.M. Twardoch, "The Chemistry and Electrochemistry Associated with the Electroplating of Group VIA Transition Metals," *Journal of Applied Electrochemistry* **17** (1987) 225-242.
4. Pierre Taxil, Jean Mahenc, "Formation of Corrosion-ressitant layers by Electrodeposition of Refractory Metals or by Alloy Electrodeposition in Molten Fluorides," *Journal of Applied Electrochemistry* **17** (1987) 261-269.
5. A. Girginov, T.Z. Tzvetkoff, M. Bojinov, "Electrodeposition of Refractory Metals (Ti, Zr, Nb, Ta) from Molten Salt Electrolytes," *Journal of Applied Electrochemistry* **25** (1995) 993-1033.
6. P.K. Tripathy, J.C. Sehra, D.K. Bose, R.P. Singh, "Electrodeposition of vanadium from a molten Salt Bath," *Journal of Applied Electrochemistry* **26** (1996) 887-890.
7. K.H. Stern, "Electrodeposition of Refractory Carbide Coatings From Fluoride Melts," *Journal of Applied Electrochemistry* **22** (1992) 717-721.
8. N. Komatsu, T. Arai, "TD Process for Carbide Coatings," *New Mater. New Process.* **1(1)** (1981), 145-150.
9. http://www.metalbheattreat.com/vanadium carbide.htm
10. John S. Wilkes, "A Short History of Ionic Liquids-From Molten Salts to Neoteric Solvents," *Green Chemistry* **4** (2002) 73-80.
11. Yasuhiko Ito, Toshiyuki Nohira, "Non-conventional Electrolytes for Electrochemical Applications," *Electrochimica Acta* 45 (2000) 2611-2622.
12. Rika Hagiwara, Yasuhiko Ito, "Room Temperature Ionic Liquids of Alkylimidazolium Cations and Fluoroanions," *Journal of Fluorine Chemistry* **105** (2000) 221-227.
13. Yuguang Zhao T.J. VanderNoot, "Review: Electrodeposition of Aluminum from nonaqueous Organic Electrolytic systems and Room Temperature Molten salts," *Electrochimica Acta* **42** (1997) 3-13.
14. Yu-Feng Lin, I.-Wen Sun, "Electrodeposition of Zinc from a Lewis Acidic Zinc Chloride-1-ethyl-3-Methylimidazolium Chloride Molten salt," *Electrochimica Acta* **44** (1999) 2771-2777.
15. Muhammad Rostom Ali, Atsushi Nishikata, Tooru Tsuru, "Electrodeposition of Aluminum-Chromium Alloys from $AlCl_3$-BPC Melt and its Corrosion and High Temperature Oxidation Behaviors," *Electrochimica Acta* **42** (1997) 2347-2354.
16. Tetsuya Tsuda, Toshiyuki Nohira, Yasuhiko Ito, "Nucleation and Surface Morphology of Aluminum-Lanthanum Alloy Electrodeposited in a $LaCl_3$-EtMeImCl Room Temperature Molten salt," *Electrochimica Acta* **47**, (2002) 2817-2822.
17. Tatsuko Takei, "The Electrodeposition of Metals from Their Trifluoroacetate-amide baths," *Electrochimica Acta* **25 (10)** (1980) 1231-1237.
18. Tatsuko Takei, "Studies on the Electrodeposition from Organic Solutions of Metals that are Difficult to deposit from Aqueous Solutions," *Surface Technology* **9 (4)** (1979) 285-302.

19. Tatsuko Takei, "Electrodeposition of Nickel from $Ni(CF_3COO)_2$-halide-MEOH Bath," *Electrochimica Acta* **23(12)** (1978) 1321-1324.
20. T. Arai and S Harper: *ASM Handbook*, Vol. 4, p. 448 (1994).
21. Glenn T. Visscher, David C. Nesting, John V. Badding, Patricia A. Bianconi, "Poly(phenylcarbyne): A Polymer Precursor to Diamond-Like Carbon", *Science* **260** (1993) 1496-1499.
22. Xingbin Yan, Tao Xu, Xiaobo Wang, Huiwen Liu, Shengrong Yang, "Microstructure and mechanical properties of hard carbon films prepared by heat treatment of a polymer on steel substrate", *Surface & Coatings Technology* **190** (2005) 206–211.
23. L.C. Olson, J.W. Ambrosek, K. Sridharan, M.H. Anderson, T.R. Allen, Materials Corrosion in Molten LiF-NaF-KF Salt, J. Fluorine Chem., 2009, 130, p 67-73, in English.
24. M.C. Brupbacher, D. Zhang, W.M. Buchta, M.L. Graybeal, Y.-R. Rhim, D.C. Nagle, J.B. Spicer, Synthesis and Characterization of Binder-Free Cr_3C_2 Coatings on Nickel-Based Alloys for Molten Fluoride Salt Corrosion Resistance, J. Nucl. Mater., 2015, 461, p 215-220, in English.
25. M.C. Brupbacher, D. Zhang, W.M. Buchta, Y.-R. Rhim, D.C. Nagle, J.B. Spicer, Post-Treatment of Plasma-Sprayed Cr_2O_3 with Methane-Containing Gas for Conversion to Binder-free Cr_3C_2, J. Therm. Spray Technol., Under Review, in English.
26. M.C. Brupbacher, D. Zhang, W.M. Buchta, Y.-R. Rhim, D.C. Nagle, J.B. Spicer, Microstructural Characterization of Hard Chromium after Carburization with Methane-Containing Gas: An Insight into High-Temperature Carbide Formation Mechanisms, In Preparation, in English.
27. N. Anacleto, O. Ostrovski, Solid-State Reduction of Chromium Oxide by Methane-Containing Gas, Metallurgical and Materials Transactions B, 35B, (2004), 609-615.
28. P. Read, D. Reeve, J. Walsh, J. Rehder, Reduction of chromites in methane-hydrogen mixtures-chromium sesquioxide, Canadian Metallurgical Quarterly, 13, (1974), 587-595.
29. M. Qayyum, D. Reeve, Reduction of chromites to sponge ferrochromium in methane-hydrogen mixtures, Canadian Metallurgical Quarterly, 15, (1976), 193-200.
30. R. Ebrahimi-Kahrizsangi, H. Monajati Zadeh, V. Nemati, Synthesis of chromium carbide by reduction of chromium oxide with methane, International Journal of Refractory Metals and Hard Materials, 28, (2010), 412-415.
31. B. Khoshandam, R. Kumar, E. Jamshidi, Producing Chromium Carbide Using Reduction of Chromium Oxide with Methane, American Institute of Chemical Engineers Journal, 52, (2006), 1094-1102.
32. L.-M. Berger, S. Stolle, W. Gruner, K. Wetzig, Investigation of the carbothermal reduction process of chromium oxide by micro- and lab-scale methods, International Journal of Refractory Metals and Hard Materials, 19, (2001), 109-121.
33. W. Gruner, S. Stolle, K. Wetzig, Formation of CO_x species during the carbothermal reduction of oxides of Zr, Si, Ti, Cr, W, and Mo, International Journal of Refractory Metals and Hard Materials, 18, (2000), 137-145.
34. G.-C. Ji, C.-J. Li, Y.-Y. Wang, W.-Y. Li, Erosion Performance of HVOF-Sprayed Cr_3C_2 NiCr Coatings, Journal of Thermal Spray Technology, 16, (2007), 557-565.
35. T. Sidhu, S. Prakash, R. Agrawal, Characterizations and hot corrosion resistance of Cr_3C_2-NiCr coating on Ni-base superalloys in an aggressive environment, Journal of Thermal Spray Technology, 15, (2006), 811-816.

36. G. Matthäus, J. Picas, A. Forn, Effect of feedstock powder size on the sliding wear behavior of thermal sprayed HVOF Cr_3C_2-NiCr coatings, Thermal Spray 2004: Advances in Technology and Application, (2004), 529-533.
37. Haynes International, Haynes 230 Alloy, (2014), URL: http://www.haynesintl.com/pdf/h3000.pdf.
38. M. Brupbacher, D. Zhang, W. Buchta, J. Spicer, D. Nagle, Formation of Molten Fluoride Salt Corrosion Resistant Coatings on Nickel-Based Alloys, ANS Transactions, 111, (2014), 584-587.
39. G. Blann, G. Vander Voort, Preparation of Thermally Sprayed Coatings!, Tech-Notes, 1, (1997).
40. C.-J. Li, A. Ohmori, Relationship Between the Microstructure and Properties of Thermally Sprayed Deposits, J. of Thermal Spray Technology, 11, (2002), 365-374.
41. S. Kuroda, T. Clyne, The Quenching Stress in Thermally Sprayed Coatings, Thin Solid Films, 200, (1991), 49-66.
42. S. Rundqvist, G. Runnsjö, Crystal Structure Refinement of Cr_3C_2, Acta Chemica Scandinavica, 23, (1969), 1191-1199.
43. M. Brupbacher, D. Zhang, M. Buchta, M. Graybeal, Y.-R Rhim, D. Nagle, J. Spicer, Synthesis and characterization of binder-free Cr_3C_2 coatings on nickel-based alloys for molten fluoride salt corrosion resistance, Journal of Nuclear Materials, In-press.
44. J. Carberry, Fluid-Solid Noncatalytic Reactions, Chemical and Catalytic Reaction Engineering, 7, (2001), 310-356.
45. P. Ramachandran, L. Doraiswamy, Modelling of noncatalytic gas-solid reactions, American Institute of Chemical Engineers Journal, 28, (1982), 881-900.
46. L. Olson, J. Ambrosek, K. Sridharan, M. Anderson, T. Allen, Materials corrosion in molten LiF-NaF-KF salt, Journal of Fluorine Chemistry, 130, (2009), 67-73.
47. S. Delpech, C. Cabet, C. Slim, G. Picard, Molten fluorides for nuclear applications, Materials Today, 13, (2010), 31-41.

Title: Carbide Coatings for Nickel Alloys, Graphite and Carbon/Carbon Composites to be used in Fluoride Salt Valves

PI Contact Info: (Dennis Nagle, Johns Hopkins University, dnagle@jhu.edu (410) 516-8970
Technical Area Workscope Identifier: B4B-2, TPOC: Timothy Burchell (ORNL), Program Manager at DOE-HQ: Brian Robinson

Purpose/Objective: To establish commercially viable technologies for the formation of refractory metal carbide coatings on nickel-based alloys, graphite, and carbon/carbon composites. Based on the molten fluoride salt corrosion test results candidate materials will be recommended for potential valve applications.

Other Personnel:
Dr. Dajie Zhang, Associate Research Engineer
Mark Buchta, Staff Engineer

Student Personnel:
Michael Brupbacher, PhD Graduate Student

Duration: 4 years

Total Funding Level: $1,183,000

Importance/Relevance: This project will determine the validity of refractory metal carbides as corrosion protectant coatings in a molten fluoride salt environment.

Logical Path:

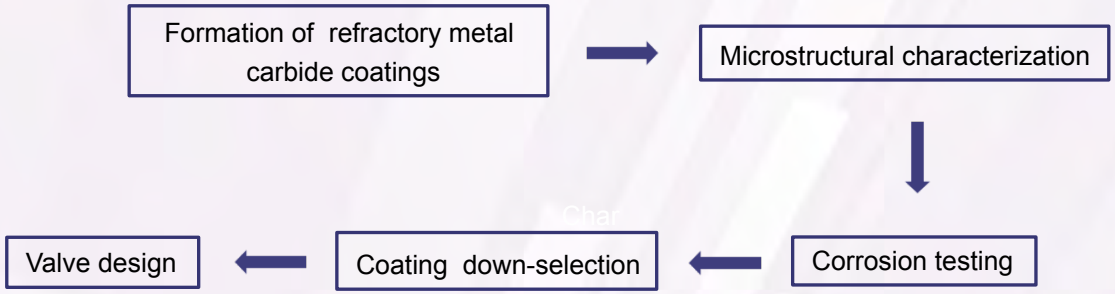

Impact Areas: This project will identify novel materials for containment of molten fluoride salts, thereby permitting the use of molten fluoride salts as both primary and secondary heat transfer media as envisioned in Gen-IV reactor concepts.

Special Tools/Methods and Facilities being used:

Experimental:
- Deposition of refractory metal on nickel-based alloys, graphite and carbon/carbon composites as coating precursors.
- Conversion (w/ methane-containing gas) of refractory metal coating precursors for carbide formation.

Facilities/Equipment:
- PANalytical X'Pert X-ray Diffractometer.
- JEOL 6700F Cold Cathode Field Emission Scanning Electron Microscope.

Sample Results:

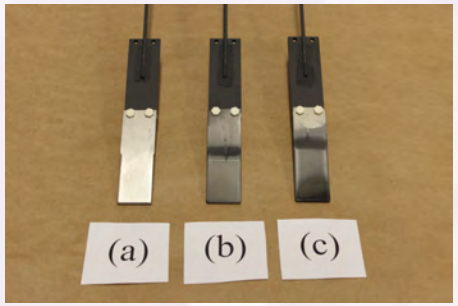

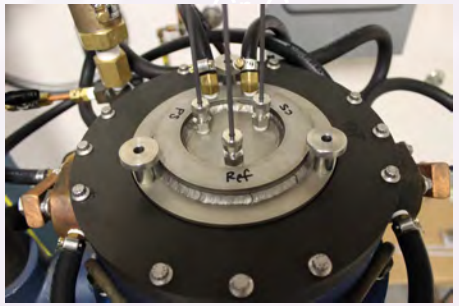

Fabricated samples undergoing testing in molten fluoride salt corrosion cell:
(a) uncoated nickel-based alloy
(b) Cr carbide coating resulting from conversion of plasma-sprayed Cr
(c) Cr carbide coating resulting from conversion of cold-sprayed Cr

Status of Deliverables:
- Development of a innovative process for the rapid formation of microporous refractory metal carbide coatings on nickel-based alloys, graphite and carbon/carbon composites.
- Design, fabrication and implementation of molten fluoride salt corrosion cell.